High-Fidelity CFD Verification Workshop 2024 Summary: Spalart-Allmaras QCR2000-R Turbulence Model

Boris Diskin*
NASA Langley Research Center, Hampton, Virginia 23681, USA

Marshall C. Galbraith[†]
Massachusetts Institute of Technology, Cambridge, Massachusetts 02139, USA

Paul Batten[‡]
Metacomp Technologies Inc., Westlake Village, California 91361, USA

Kevin R. Holst[§]
University of Tennessee, Knoxville, Tennessee 37996, USA

Yi Liu[¶] and Mohagna J. Pandya[‖]
NASA Langley Research Center, Hampton, Virginia 23681, USA

Cosimo Tarsia Morisco**
GammaO, Equipe Inria-ONERA – Centre Inria de Saclay, Université Paris-Saclay, F-91120 Palaiseau, France
National Institute of Aerospace, Hampton, Virginia 23666, USA

Anup Pandey[††]
Institute of Engineering, Tribhuvan University, Lalitpur, Bagmati 44700, Nepal

This paper summarizes solutions submitted for the Reynolds-averaged Navier-Stokes (RANS) test suite of the High-Fidelity CFD Verification Workshop. The goal of the workshop is to establish standards for verification of computational fluid dynamics (CFD) approaches to simulations of steady and unsteady turbulent flows. The RANS verification studies focus on a one-equation Spalart-Allmaras model with quadratic constitutive relation and rotation correction, SA-neg-QCR2000-R. The verification test cases are a two-dimensional subsonic flow around a Joukowski airfoil, a three-dimensional subsonic flow around an extruded NACA 0012 wing in a tunnel, and a subsonic flow around a wing-body configuration developed for verification of solvers participating in the 5th High-Lift Prediction Workshop. The turbulence-model formulation, geometry, flow conditions, grids, and reference solutions are described in detail. Solutions for the test cases are computed by seven established CFD solvers on adapted- and fixed-grid families using different discretization approaches. While some noticeable differences between solutions remain, the results achieved by contributing solvers show that different solutions computed for the same RANS model on different grid families can converge to a common limit with grid refinement. The apparent requirements for grid convergence are a well designed family of grids that provide sufficient resolution in important areas and a strong solver capable of deep iterative convergence on each grid. For each test case in the study, the variation between aerodynamic forces computed by different solvers on the finest grids of different families is less than 2%.

*Senior Research Scientist, Computational Aerosciences Branch, Associate Fellow AIAA

[†]Principal Research Engineer, Department of Aeronautics & Astronautics, Senior Member AIAA

[‡]Principal Scientist, Senior Member AIAA

[§]Research Professor, Electrical Engineering and Computer Science, Senior Member AIAA

[¶]Research Aerospace Engineer, Computational Aerosciences Branch, Senior Member AIAA

[‖]Research Aerospace Engineer, Configuration Aerodynamics Branch, Senior Member AIAA

**Research Engineer

[††]Research Scholar, Department of Mechanical and Aerospace Engineering, Student Member AIAA

Nomenclature

b	=	l_2 norm of velocity gradient tensor
c_*	=	turbulence-model constants
d	=	distance to nearest wall or total drag coefficient in two dimensions, subscript
dp	=	pressure drag coefficient in two dimensions, subscript
dv	=	viscous drag coefficient in two dimensions, subscript
e	=	specific internal energy
f, x	=	x component of skin-friction coefficient, subscript
h	=	grid element characteristic length
i, j, k	=	dimension indices, subscript
o	=	normalized antisymmetric rotation tensor
p	=	pressure
q	=	heat flux
t	=	time
u	=	velocity vector
x, y, z	=	spatial coordinates
y^+	=	distance from first grid layer to wall in inner variables
C_*	=	aerodynamic coefficients
C	=	cost model, degrees of freedom in grid
D	=	dimensions or total drag coefficient in three dimensions, subscript
DOF	=	degrees of freedom for grid
Dp	=	pressure drag coefficient in three dimensions, subscript
Dv	=	viscous drag coefficient in three dimensions, subscript
E	=	total specific energy
$\mathcal{E}$	=	error model
$\mathcal{M}$	=	continuous metric field
L	=	total lift coefficient in three dimensions, subscript
M	=	Mach number
N	=	target upper bound of degrees of freedom for adapted grid
P	=	polynomial degree or pressure, subscript
Pr	=	meanflow Prandtl number
Pr_t	=	turbulence-model Prandtl number
Re_L	=	Reynolds number based on distance L
S	=	strain tensor or strain-rate magnitude
S^*	=	Sutherland's law constant
T	=	temperature
α	=	angle of attack
γ	=	ratio of specific heats
δ	=	Kronecker function
ϵ	=	relative difference
η	=	local error estimate
κ	=	UMUSCL constant or von Kármán constant
μ	=	molecular dynamic viscosity
μ_t	=	turbulent eddy viscosity
ν	=	kinematic viscosity
$\hat{\nu}$	=	Spalart-Allmaras working turbulence variable
ρ	=	fluid density
σ	=	laminar viscous stress tensor
τ	=	Reynolds stress tensor
∂	=	partial derivative
Ω	=	magnitude of vorticity or computational domain

I. Introduction

A High-Fidelity Computational Fluid Dynamics (CFD) Verification Workshop (HiFiCFD) was held at the American Institute of Aeronautics and Astronautics (AIAA) Science and Technology Forum (SciTech) in 2024. The goal of the workshop was to establish standards for verification of computational fluid dynamics (CFD) approaches to simulation of steady and unsteady turbulent flows. This workshop is a successor to a series of community activities that have been supported by AIAA for a number of years. The immediate predecessor is the High-Fidelity CFD Workshop [1], conducted at the 2022 AIAA SciTech. Other activities include a series of AIAA special sessions and international workshops on high-order methods (e.g., Refs. [2, 3]), and a series of AIAA special sessions and publications on Reynolds-averaged Navier-Stokes (RANS) solver technology [4, 5]. This year, a special session at the AIAA 2024 Aviation Forum features presentations on verification of CFD solvers for wall-modeled large-eddy simulations, simulations on moving and deforming grids, simulations of shock-dominated flows, and RANS simulations. Distinct from validation studies that focus on the ability of model equations to represent correct physical behavior, verification studies focus on correctness of implementation of specific models. In the absence of known exact solutions, verification is accomplished through comparison of simulations conducted by different codes using well-defined verification metrics.

The importance of verification of RANS solvers has been recognized for many years. The Turbulence Modeling Resource (TMR) website [6] supported at the NASA Langley Research Center (LaRC) assists in verification of implementations of turbulence models by providing reference solutions for benchmark flows. Reference solutions for the negative version (SA-neg) [7] of the one-equation linear Spalart-Allmaras (SA) turbulence model [8] have been computed in Refs.[5, 9] and posted on the TMR website. The considered test cases included a two-dimensional (2D) flat-plate configuration, the NACA 0012 airfoil, three-dimensional (3D) bump and hemisphere-cylinder configurations, and the ONERA M6 wing. In 2021, a collaboration of researchers computed reference solutions for the SA-neg model with a quadratic constitutive relation (QCR) [10] for a SciTech special session, High-Fidelity CFD Preworkshop [11]. The QCR is needed for SA-based RANS simulations of corner flows because normal stress differences induce flowfield behavior that cannot be captured with linear eddy-viscosity models that rely on the Boussinesq assumption. The benchmark cases for verification of the SA-neg-QCR2000 model included a 2D Joukowski airfoil, a 3D supersonic flow through a long duct with a square cross-section, and a 3D flow over the NASA juncture-flow model [12].

The collaborative verification studies conducted in the past year and reported in this paper enhance the SA-neg-QCR2000 model with a rotation correction proposed in Refs. [13, 14]. The rotation correction mitigates generation of spurious eddy viscosity within a mature vortex. The target model is referred to as the SA-neg-QCR2000-R turbulence model according to the naming convention of the TMR website. As an outcome of the current study, the TMR description of this rotation correction has been clarified and updated, especially in relation to the SA-neg formulation. Additional modifications have been recently proposed in Ref. [15] to improve differentiability of the correcting function in the production term. The presented verification study focuses on the version of the rotation correction documented on TMR. Nevertheless, new modifications will be pointed out wherever appropriate. The three test cases include a 2D flow around a Joukowski airfoil, a 3D flow around an extruded NACA 0012 wing in a tunnel, and a 3D flow around a wing-body high-lift common research model (CRM-HL-WB) developed for verification of CFD solvers applied to high-lift aerodynamics research. The CRM-HL-WB case is a joint verification test case with the Fifth High-Lift Prediction Workshop (HLPW-5) [16]. Solutions for the test cases are computed using well established RANS solvers. Families of consistently refined unstructured grids have been generated for each case and are available to the community through the HiFiCFD website [17]. Descriptions of the verification cases, the SA-neg-QCR2000-R turbulence model, and preliminary solutions computed with two codes have been reported in Ref. [18]. In the current paper, the test cases and grids have been adjusted to facilitate grid convergence, and seven solvers using different discretization approaches are used to compute and compare well-converged solutions on the grid families that include grids with more degrees of freedom.

The material in this paper is presented in the following order. Section II describes the SA-neg-QCR2000-R turbulence model. Section III introduces the solvers participating in the verification study. Sections IV, V, and VI present three verification cases and the corresponding solutions. Section VII summarizes results obtained in the study and provides recommendations. Auxiliary studies on the drag trends in the low-Mach limit and effects of the turbulence-model boundary conditions at slip walls are reported in appendices.

II. Reynolds-Averaged Navier-Stokes Model

The 3D compressible unsteady Navier-Stokes equations are conservation laws for mass, momentum, and energy. Following the TMR conventions and using the Einstein notation of summation over the repeated indexes, the equations

can be written as

$$\begin{cases} \partial_t \rho + \partial_j \left(\rho u_j \right) = 0, \\ \partial_t \left(\rho u_i \right) + \partial_j \left(u_j \rho u_i \right) + \partial_i p = \partial_j \sigma_{ji} + \partial_j \tau_{ji}, \\ \partial_t \left(\rho E \right) + \partial_j \left(u_j (\rho E + p) \right) = \partial_j \sigma_{jk} u_k + \partial_j \tau_{jk} u_k - \partial_j q_j. \end{cases} \tag{1}$$

Here $\partial_j, j = 1, 2, 3$ are the spatial derivatives in the x, y, and z directions, respectively; ∂_t is the time derivative; $\rho, \rho u_i$, and ρE are conserved variables representing the density, the momentum, and the total energy per unit volume; u_i are the velocity components, p is the static pressure, and E is the total specific energy that is defined as a sum of specific internal energy and specific kinetic energy.

$$E = e + \frac{u_i u_i}{2}. \tag{2}$$

Primitive variables are ρ, u_i, and p. For a perfect gas, the variables are connected through the following relation:

$$p = (\gamma - 1) \left(\rho E - \frac{\rho u_i u_i}{2} \right), \tag{3}$$

where $\gamma = 1.4$ is the specific heat ratio. The laminar viscous stress tensor is defined as

$$\sigma_{ij} = 2\mu \left(S_{ij} - \frac{1}{3} \partial_k u_k \delta_{ij} \right), \tag{4}$$

where

$$S_{ij} = \frac{1}{2} \left(\partial_i u_j + \partial_j u_i \right) \tag{5}$$

is the strain tensor,

$$\delta_{ij} = \begin{cases} 1 & \text{for } i = j \\ 0 & \text{for } i \neq j \end{cases} \tag{6}$$

is the Kronecker delta, and μ denotes the molecular dynamic viscosity. For a perfect gas, μ is governed by Sutherland's law

$$\frac{\mu}{\mu_{\text{ref}}} = \left(\frac{T}{T_{\text{ref}}} \right)^{\frac{3}{2}} \left(\frac{T_{\text{ref}} + S^*}{T + S^*} \right), \tag{7}$$

where T is the temperature, the reference viscosity μ_{ref} is assumed at the reference temperature T_{ref}, and $S^* = 198.6 \, °\text{R}$. For a turbulent flow, the Reynolds stress tensor, τ_{ij} is modelled. The linear SA model uses the Boussinesq approximation

$$\tau_{ij} = 2\mu_t \left(\frac{1}{2} \left(\partial_i u_j + \partial_j u_i \right) - \frac{1}{3} \partial_k u_k \delta_{ij} \right), \tag{8}$$

where μ_t is a turbulent eddy viscosity. The heat flux is written as

$$q_j = \frac{1}{(\gamma - 1)} \left(\frac{\mu}{Pr} + \frac{\mu_t}{Pr_t} \right) \partial_j T, \tag{9}$$

the meanflow and turbulence-model Prandtl numbers are $Pr = 0.72$ and $Pr_t = 0.9$, respectively.

Following the formulation presented at the TMR website, the SA model is given as

$$\partial_t \hat{v} + u_j \partial_j \hat{v} = c_{b1} \left(1 - f_{t2} \right) \hat{S} \hat{v} + \left[c_{w1} f_w - \frac{c_{b1}}{\kappa^2} f_{t2} \right] \left(\frac{\hat{v}}{d} \right)^2 - \frac{1}{\sigma} \left[\partial_j \left((v + \hat{v}) \left(\partial_j \hat{v} \right) \right) + c_{b2} \left(\partial_j \hat{v} \right) \left(\partial_j \hat{v} \right) \right] = 0. \tag{10}$$

The boundary conditions are defined as

$$\hat{v}_{\text{wall}} = 0, \qquad \hat{v}_{\text{farfield}} = 3v_{\text{ref}}. \tag{11}$$

Here, $\hat{v}$ is the turbulence working variable, d is the distance to the wall, including a tangency wall (perfect slip inviscid boundary conditions), $v = \mu/\rho$ is the kinematic viscosity, and v_{ref} is the reference kinematic viscosity. The turbulent eddy viscosity is computed as

$$\mu_t = \rho \hat{v} f_{v1}. \tag{12}$$

4

In the original reference [8], $\hat{S}$ in the production term of the SA model is defined as follows

$$\hat{S} = \Omega + \bar{S}, \qquad \bar{S} = \frac{\hat{\nu}}{\kappa^2 d^2} f_{v2}. \tag{13}$$

Here, Ω is the magnitude of the vorticity vector

$$\Omega = \sqrt{2W_{ij}W_{ij}}; \qquad W_{ij} = \frac{1}{2}\left(\partial_j u_i - \partial_i u_j\right). \tag{14}$$

To avoid numerical problems with $\hat{S} \leq 0$, Ref. [7] suggests the following modifications

$$\hat{S} = \Omega + \frac{\Omega\left(c_2^2\Omega + c_3\bar{S}\right)}{(c_3 - 2c_2)\,\Omega - \bar{S}} \text{ when } \bar{S} < -c_2\Omega, c_2 = 0.7, c_3 = 0.9. \tag{15}$$

Other terms appearing in Eq. 10 are defined as follows.

$$f_{v1} = \frac{\chi^3}{c_{v1}^3 + \chi^3}, \chi = \frac{\hat{\nu}}{\nu}, f_{v2} = 1 - \frac{\chi}{1 + \chi f_{v1}}, f_w = g\left[\frac{1 + c_{w3}^6}{g^6 + c_{w3}^6}\right]^{\frac{1}{6}},$$
$$g = r + c_{w2}\left(r^6 - r\right), r = \min\left[\frac{\hat{\nu}}{\hat{S}\kappa^2 d^2}, 10\right], f_{t2} = c_{t3}e^{-c_{t4}\chi^2}. \tag{16}$$

The constants are

$$\kappa = 0.41, \sigma = \frac{2}{3}, c_{b1} = 0.1355, c_{b2} = 0.622, c_{t3} = 1.2, c_{t4} = 0.5,$$
$$c_{v1} = 7.1, c_{w1} = \frac{c_{b1}}{\kappa} + \frac{1 = c_{b2}}{\sigma}, c_{w2} = 0.3, c_{w3} = 2. \tag{17}$$

The standard SA model is defined for $\hat{\nu} \geq 0$. Reference [7] extends the model formulation to $\hat{\nu} < 0$; the extended formulation is referred to as the SA-neg model. For $\hat{\nu} < 0$, the following equation is solved.

$$\partial_t \hat{\nu} + u_j \partial_j \hat{\nu} = c_{b1}\left(1 - c_{t3}\right)\Omega\hat{\nu} - c_{w1}\left(\frac{\hat{\nu}}{d}\right)^2 - \frac{1}{\sigma}\left[\partial_j\left((\nu + \hat{\nu}f_n)\left(\partial_j\hat{\nu}\right)\right) + c_{b2}\left(\partial_j\hat{\nu}\right)\left(\partial_j\hat{\nu}\right)\right] = 0. \tag{18}$$

Function f_n is defined as follows.

$$f_n = \frac{c_{n1} + \chi^3}{c_{n1} - \chi^3}, \qquad c_{n1} = 16. \tag{19}$$

The turbulent eddy viscosity is set to zero for $\hat{\nu} < 0$. A revised implementation of the SA-neg formulation [19] results in a slight modification in the last term in Eq. 18

$$\partial_t \hat{\nu} + u_j \partial_j \hat{\nu} = c_{b1}\left(1 - c_{t3}\right)\Omega\hat{\nu} - c_{w1}\left(\frac{\hat{\nu}}{d}\right)^2 - \frac{1}{\sigma}\left[\partial_j\left((\nu + (1 + c_{b2})\hat{\nu}f_n)\left(\partial_j\hat{\nu}\right)\right) - c_{b2}\hat{\nu}f_n\partial_j\left(\partial_j\hat{\nu}\right)\right] = 0. \tag{20}$$

In the QCR2000 formulation [10], the turbulent stress tensor is modelled using QCR and nonlinear interactions between the Boussinesq-based turbulent stress tensor defined in Eq. 8 and a normalized antisymmetric rotation tensor that is defined as

$$o_{ij} = \frac{2}{b}W_{ij}. \tag{21}$$

Here, W_{ij} is defined in Eq. 14 and b is the l_2-norm of the velocity gradient tensor, $\partial_i u_j$,

$$b = \sqrt{\left(\partial_i u_j\right)\left(\partial_i u_j\right)}. \tag{22}$$

The rotation tensor is set to zero when $b = 0$. The QCR turbulent stress tensor is computed as follows.

$$\tau_{ij,QCR} = \tau_{ij} - c_{cr1}\left[o_{ik}\tau_{kj} - \tau_{ik}o_{kj}\right], \qquad c_{cr1} = 0.3. \tag{23}$$

The meanflow stress tensor remains unchanged.

In the SA-R variant of the SA model with the rotation correction [13, 14], $\hat{S}$ in the production term is modified as

$$\hat{S} + c_{\text{rot}}\min\left(0, S - \Omega\right), \tag{24}$$

5

S is the magnitude of the strain-rate tensor defined as

$$S = \sqrt{2S_{ij}S_{ij}}, \tag{25}$$

S_{ij} is defined in Eq. 5. If the strain magnitude is less than the vorticity magnitude, $S < \Omega$, and $c_{\text{rot}} > 1$, the production term may become negative and suppress eddy viscosity, which is considered as a desirable property in case of a solid body rotation. References [13–15] recommend $c_{\text{rot}} = 2$. Computations reported in Refs. [18, 20] use $c_{\text{rot}} = 1$. Note that all models based on the SA-neg version of the SA model [7] benefit from smooth transition through $\hat{\nu} = 0$; therefore, it would be preferable to have the production term as $c_{b1} (1 - c_{t3}) (\Omega + c_{\text{rot}} \min (0, S - \Omega)) \hat{\nu}$ in the negative branch of the SA-neg-R model. On the other hand, the SA-neg approach does not allow a negative production term for $\hat{\nu} < 0$. For the current verification campaign, the negative branch uses the absolute value of the production term,

$$c_{b1} (1 - c_{t3}) |\Omega + c_{\text{rot}} \min (0, S - \Omega)| \hat{\nu}, \tag{26}$$

and $c_{\text{rot}} = 1$ is selected. These choices ensure C4 continuity (continuity of the function and its first four derivatives) for the production term in the transition through $\hat{\nu} = 0$. Previous attempts to solve equations with $c_{\text{rot}} = 2$ were not successful; residuals were not converged to machine-zero levels. Lack of iterative convergence was attributed to insufficient smoothness of the transition through $\hat{\nu} = 0$. Only C0 continuity was provided, i.e., the production term remained continuous, but its derivatives were not. Ref. [15] replaces the min-function used in the definition of the rotation correction, Eq. 24, with a differentiable approximation in the positive branch and uses the SA-neg equation 18 in the negative branch. This formulation results in C0 continuity.

III. Solvers

A. CFD++

CFD++ is a well-validated general-purpose commercial software suite developed and disseminated by Metacomp Technologies, Inc. CFD++ is based on a grid-transparent methodology applicable to arbitrary grids [21]. Although nominally a cell-centered, finite-volume approach, by default CFD++ uses a vertex-based least-squares polynomial reconstruction that preserves linearity regardless of mesh skew. This is a sufficient condition for CFD++ to formally maintain second-order accuracy irrespective of local mesh quality. CFD++ also has low-Mach-number preconditioning available, which is used for each of the CFD++ results presented in this paper. One additional numerical option that is used for these calculations is a low-diffusion limiter with a wider stencil to determine broader (vertex-neighbor) bounds for the polynomial limiter function. This limiter tends to activate less frequently than conventional limiters based on face-neighbor data, resulting in reduced dissipation and also reduced non-linearity, which can sometimes help achieve deeper convergence. Turbulence-model equations in CFD++ are treated with a fully second-order accurate scheme, but these are also subject to the same limiter function in order to ensure monotonicity. CFD++ contains an approximate (Poisson-solver based) method as well an an exact calculator for the wall distances required by the SA model. To avoid any uncertainties, the exact distance calculator was used in all presented CFD++ solutions.

The CFD++ implicit scheme linear solver is an agglomeration algebraic multigrid, sensitized to both the mesh connectivity and the local coefficients of the discretized equations. The source terms of the turbulence-model equation are subject to a semi-segregated, Patankar-type linearization, in which net negative sources are treated implicitly in order to provide a finite numerical rate of decay that preserves positivity for physically non-negative quantities. This applies to the standard SA model, but is relaxed for the SA-neg model since its working variable, $\hat{\nu}$, is allowed to become locally negative.

We consider the SA-neg model as a fairly ingenious invention for discrete numerical methods that can inevitably (with more complete linearization and larger time-steps), lead to a loss of positivity. CFD++ did not have the SA-neg model available before 2024; the first HiFiCFD solutions have been computed using the standard SA model. The subsequent addition of the SA-neg model has not changed the results, but it has, in some instances, aided in convergence. From the CFD++ experience, the SA-neg model seems to generally be a net positive for the convergence of the $\hat{\nu}$ variable, but the improvement in the meanflow residual convergence was found to be less consistent.

B. COFFE

The Conservative Field Finite Element (COFFE) solver within HPCMP CREATE™-AV Kestrel [22] is an unstructured, continuous Galerkin flow solver that utilizes a streamline upwind Petrov-Galerkin (SUPG) approach [23–28] for

stabilization. `COFFE` uses linear or quadratic Lagrangian basis functions for the fully-coupled meanflow and turbulence-model equations, which provide 2nd or 3rd-order spatial discretization accuracy, respectively, and time discretization is accomplished using a selection of singly diagonally implicit Runge-Kutta methods [29, 30]. Pseudo-time continuation (PTC) is used to solve the steady, nonlinear system of equations via Newton's method. Solution updates are computed by solving a linear system using the generalized minimal residual (GMRES) method [31] preconditioned with an incomplete lower-upper (LU) factorization. Automatic differentiation through operator overloading is used to compute the exact linearization of the coupled residuals for the linear system. Homotopy continuation is used to aid in nonlinear convergence. With this technique, artificial diffusion is applied to the governing equations at the start of the simulation. Over time, this diffusion is reduced and eliminated, and the residuals for the final solution are driven down to machine zero. This approach helps the solver handle non-physical flow phenomena that materialize as the solution traverses the nonlinear space.

The SA-neg turbulence model is available with `COFFE`, along with options for QCR2000 and the -R rotation correction variant, all of which are the focus of this effort. The standard implementation of the rotation correction within `COFFE` uses $c_{rot} = 2$. This coefficient is not modifiable by users, so a custom build was created with $c_{rot} = 1$ specifically for this work.

C. FUN3D

`FUN3D` [32] is an unstructured-grid, node-centered flow solver developed and supported at NASA LaRC; `FUN3D` is widely used for high-fidelity analysis and adjoint-based optimization of complex turbulent flows [33–35]. Recently `FUN3D` has been successfully ported to advanced computing architectures [36–38]. There are two types of discretizations available in `FUN3D`, a second-order accurate, finite-volume scheme [39] and a SUPG continuous finite-element scheme [28]. The finite-volume discretization used in this paper is accomplished on general unstructured grids that may contain tetrahedra, pyramids, prisms, and hexahedra. The residuals are evaluated on a set of median-dual control volumes centered at grid points. Edge-based inviscid fluxes are computed at edge midpoints using an approximate Riemann solver. In the current solutions, Roe's flux-difference splitting (FDS) [40] is used. For second-order accuracy, density, pressure, and velocity are reconstructed by an unstructured monotonic upstream-centered scheme for conservation laws (UMUSCL) [41, 42]. UMUSCL parameter $\kappa = 0.5$ is used in all `FUN3D` computations reported herein. The UMUSCL gradient is computed at grid points using the unweighted least-squares method and the edge-neighbor stencil. No limiters are used in this study. The spatial discretization of the turbulence model uses a first-order accurate upwind convection scheme.

For the discretization of viscous fluxes, the Green–Gauss theorem is used to compute cell-based gradients. On tetrahedra, this approach is equivalent to a Galerkin approximation [43]. For nontetrahedral cells, cell-based Green–Gauss gradients are combined with edge-based gradients [44–46] to improve stability of viscous operators and prevent odd–even decoupling. In solutions computed in this paper, the face-tangent augmentation [45, 46] is used. The diffusion term in the turbulence model is handled similarly; the revised implementation of the SA-neg model [19] ensuring positive discrete diffusion coefficients is used. In the implementation of the QCR correction [10], the antisymmetric normalized rotation tensor is computed using the cell-based gradients. The QCR fluxes are added in a cell loop. The vorticity-based source term for the turbulence model is computed using velocity gradients evaluated by the Green–Gauss method on dual control volumes.

For solutions computed in this paper, a strong nonlinear solver, hierarchical adaptive nonlinear iteration method (HANIM) [34], is used. HANIM is based on a hierarchy of modules including a preconditioner, a matrix-free linear solver, realizability check, nonlinear control, and a module for adapting the pseudo-time term that is controlled by a Courant–Friedrichs–Lewy (CFL) number. The HANIM preconditioner uses a defect-correction method with an approximate Jacobian. The meanflow and turbulence-model Jacobians are decoupled. The approximate Jacobian for the meanflow equations is formed using the linearization of the first-order accurate inviscid fluxes and the second-order accurate viscous fluxes. The approximate Jacobian for the SA-neg model includes contributions from the convection, diffusion, and source terms. The exact linearization is used for the convection and diffusion terms. The preconditioner equations are relaxed using point-implicit Gauss–Seidel (GS) sweeps with multicolor ordering. The matrix-free linear solver [47–49] uses Fréchet derivatives and a generalized conjugate residual (GCR) method [48] from the family of Krylov methods. HANIM prescribes the residual reduction targets for the preconditioner, the GCR solver, and nonlinear solution updates and specifies the maximum number of GS iterations allowed in the preconditioner and the maximum number of search directions to be used in the GCR solver. HANIM increases the CFL number if all the HANIM modules have reported success. If any of the modules fails, HANIM discards the correction and aggressively reduces the CFL

number.

D. SANS

The Massachusetts Institute of Technology (MIT) Solution Adaptive Numerical Simulator (SANS) code base includes both stabilized continuous (CG) and discontinuous (DG) Galerkin finite-element methods. In this paper, solutions of the coupled meanflow and turbulence-model equations are computed using a variational multiscale method with discontinuous subscales [50, 51]. A PTC damped Newton's method (with a complete linearization of the residuals) is utilized to solve the nonlinear Finite-Element Method (FEM) system of equations. The PTC method enhances Newton's method by employing a local time step for each element based on factors such as characteristic speed, element size, and CFL number. As the CFL number approaches infinity, each PTC iteration becomes equivalent to a pure Newton step.

Unsteady residuals are reduced by a line search performed for each PTC update. Direct LU-factorization is used to solve the linear system at each PTC iteration, and the same linear solver is utilized for solving the adjoint system. The residuals of all linear systems are driven to effectively machine zero. Convergence of the nonlinear system is considered achieved when the L^2-norm of residuals falls below 8×10^{-12} for each partial differential equation [52].

The Metric Optimization via Error Sampling and Synthesis (MOESS) mesh adaptation framework is used to generated adapted meshes in SANS [53–56]. The meshes are provably optimal [56] such that the output error indicator is minimized for a given cost. The dual weighted residual method [57] provides an error approximation via an adjoint for the output functional of interest, such as drag, which is subsequently localized to enable the adaptation process to focus on regions with significant output error. As it is impractical to optimize the discrete mesh directly, optimization is instead conducted on a continuous metric field: a smooth field consisting of symmetric positive definite matrices $\mathcal{M}(x)$ [58]. The MOESS mesh-adaptation problem in continuous form is stated as: find the optimal metric field $\mathcal{M}^*$ such that

$$\mathcal{M}^* = \arg\min_{\mathcal{M} \in \mathcal{M}(\Omega)} \mathcal{E}(\mathcal{M}), \quad \text{subject to } C(\mathcal{M}) \leq N \tag{27}$$

where $\mathcal{E}$ and C are surrogate models for error and cost, respectively. C represents the number of degrees of freedom in the mesh, and is bounded by some target upper bound N. The error model is obtained from the sum of local error contributions:

$$\mathcal{E}(\mathcal{M}) = \int_{\Omega} \eta(\mathcal{M}(x), x) \, dx \tag{28}$$

where the local error model, η, is assumed to be only a function of the local metric.

The resulting optimized metric field is then passed to a grid generator (e.g., EPIC [59], feflo.a [60], refine [61], or avro [62]) for construction of a new grid, and the adaptation process is then repeated. The resulting solutions have controlled discretization error with quantitative estimates of these errors. The entire adaptation process can begin with an initial grid that does little more than fill space with no requirements on resolving relevant flow features such as shocks or boundary layers. These features will be 'discovered' and adequately resolved during the adaptation process. This effectively eliminates the labor-intensive and subjective human-in-the-loop grid generation effort from the overall solution process, resulting in significant wall clock savings as well as grids that are tailored for each flow case.

E. USM3D-ME

USM3D-ME [63–67] is a second-order accurate, finite-volume, cell-centered, mixed-element, unstructured-grid CFD solver that is developed at NASA LaRC. USM3D-ME is a successor to the USM3D solver of the NASA Tetrahedral Unstructured Software System (TetrUSS) [68] that, for many years, served as a reliable computational aerodynamic analysis tool for U.S. government, industry, and academia [68–74]. The extension to mixed-element grids improved the accuracy, efficiency, and robustness of numerical simulations by allowing flow-aligned anisotropic hexahedral or prismatic cells in boundary layers. Several important features improve the USM3D-ME accuracy, efficiency, and robustness. The features include: (1) a fully-implicit formulation that is entirely based on cell-centered solutions; (2) a compact nodal-averaging scheme for efficient parallelization; (3) a more consistent Jacobian used by the USM3D-ME preconditioner; (4) an adaptive face-based catastrophic limiter for improved robustness; (5) a revised implementation of the SA-neg turbulence model that ensures positive diffusion coefficients [19] and improves efficiency and robustness. A strong nonlinear solver, HANIM, has been implemented in USM3D-ME [64–67] to increase convergence rates and overcome instabilities occurring in transient solutions. HANIM parameters are tuned to increase robustness and reduce time to solution. USM3D-ME has been extensively used in NASA projects and has provided increased solution throughput [75]. The following are solver choices made for solutions computed in this study.

1) Turbulence model is SA-neg-QCR2000-R.
2) Meanflow inviscid fluxes use Roe's FDS scheme [40] and second-order accurate UMUSCL ($\kappa = 0$) reconstruction with no limiters.
3) Turbulence-model convection term is upwind and first-order accurate.
4) Cell gradients for meanflow inviscid terms are based on the Green–Gauss method with nodal solutions.
5) Face gradients for meanflow and turbulence-model diffusion terms use Mitchell's method [76, 77].
6) Meanflow diffusion terms are second-order accurate.
7) Turbulence-model diffusion term is second-order accurate; the revised implementation [19] is used.
8) Cell gradients for the SA-model source term are computed from arithmetically-averaged face gradients.
9) Prandtl numbers for diffusion fluxes are 0.72 for meanflow and 0.90 for the turbulence model.
10) Preconditioner residual reduction target is 0.1.
11) Maximum number of preconditioner iterations is 500.
12) GCR residual reduction target is 0.2.
13) Maximum number of GCR search directions is 50.
14) Meanflow approximate-Jacobian inviscid terms use linearization of the first-order accurate Roe's FDS fluxes.
15) Approximate-Jacobian diffusion terms use thin-layer approximation.
16) Initial conditions are based on freestream flow.
17) 200 iterations with first-order accurate inviscid fluxes are conducted before switching to the target second-order accurate discretization.

F. WOLF

WOLF [78–81] is a node-centered, finite-volume/finite-element RANS solver originally developed for unstructured meshes. Convective fluxes are discretized by an edge-based finite-volume method on a median-dual mesh, while the viscous fluxes are discretized using the P1-Galerkin method. Specifically, an HLLC (Harten-Lax-van Leer-Contact) approximate Riemann solver [82] is used in concert with a low-dissipation, second-order accurate UMUSCL scheme using a combination of centered edge gradient and upwind finite-element gradient[83, 84]. The extension to quadrilateral elements has been introduced in Ref [85]. This formulation involves the evaluation the finite-element gradient at grid points and provides the same accuracy as the baseline version when the upwind/downwind quadrilateral elements are aligned with the attached edge. The Approximated Finite Element (APFE) method [86] is used to discretize the viscous fluxes on quadrilateral elements. A global second-order accuracy is guaranteed on fully triangular/tetrahedral and fully quadrilateral regions. Simulations on three-dimensional mixed-element fixed grids use an extension of this strategy to prisms and pyramids, which was proposed in Refs. [87, 88]. Time integration is accomplished via a backward Euler scheme for implicit temporal discretization. Specifically, at each time step, the RANS equations are approximately solved using a Symmetric Gauss–Seidel (SGS) method with a local time stepping. An implicit, loosely-coupled algorithm is used to integrate the meanflow and turbulence-model equations. In the context of this work, the SA-neg-QCR2000-R model was implemented and used.

Grid adaptation is performed on purely simplex meshes. In this process, local size and anisotropy are prescribed using a metric field [81, 89]. In this context, a tetrahedron is considered *unit* according to a metric if all its edges have unit length in this metric. Similarly, a grid that is unit for a given metric field is composed of unit elements in this metric. This condition establishes a duality between grids and metrics: a Riemann metric field can be seen as the continuous counterpart of a grid. The reader can refer to Refs. [90, 91] for more details. In this way, the grid generation is recast as generation of a uniform unit mesh in the prescribed metric space. The optimization of the continuous metric $\mathcal{M}$ is performed according to Eq. 27. The optimal metric field $\mathcal{M}_{\text{Opt}}$ is deduced from the solution on a grid or from the solution and an adjoint state with different error estimates [81]. The optimal metric field is used to prescribe the next adapted grid. In practice, metrics computed from numerical solutions are likely irregular and need to be smoothed through a gradation process to improve the quality of the adapted mesh [92, 93]. WOLF can provide metrics for either *multiscale* or *goal-oriented* error estimates. The *multiscale* error estimate aims at minimizing the interpolation error in the L^p norm of a given sensor for a given number of degrees of freedom. The *goal-oriented* error estimate minimizes the error of a given engineering output functional for a given number of degrees of freedom. The latter algorithm is more complex than the former because it requires a robust adjoint solver and a proper differentiation of the output functional [81].

All the adaptive-grid simulations shown in this work are performed using the grid-adaptive solution platform composed of WOLF, the anisotropic local remeshing software Feflo.a [60, 94–96], and the field interpolator Interpol

[97, 98]. Each step of the adaptation process is detailed in Ref [99].

G. OpenFOAM

OpenFOAM [100] is an open-source toolbox widely used for continuum problems. It uses a cell-centered finite-volume formulation for CFD and provides flexibility of using features developed by a user in addition to the native solvers. The native package of OpenFOAM has only the SA-noft2 turbulence model. The SA-neg-QCR2000-R turbulence model is implemented starting with the existing SA-noft2 implementation. The native OpenFOAM solvers, rhoSimpleFoam, rhoPimpleFoam, and rhoSonicFoam, were not able to provide the desired accuracy converging the pressure drag to higher values compared to the truth value. The SIMPLE (Semi-Implicit Method for Pressure Linked Equations)[101] and PIMPLE (combines PISO (Pressure Implicit with Splitting of Operators)[102] and SIMPLE method) solvers were observed to be highly unstable on the skewed and non-orthogonal cells. The stability was better with the use of a pseudo-transient formulation rather than in the absence of time derivative terms but still resulted in a higher pressure drag. OpenFOAM has multiple methods for the wall distance computation, namely: mesh-wave, Poisson, and exact distance. The mesh-wave method is accurate for the orthogonal and non-skewed cells but is very poor with skewed and non-orthogonal cells. An optional wall-normal correction is available with the mesh-wave method but still could not provide an accurate wall distance for the workshop meshes. The exact distance method is much more precise than the mesh-wave method but is more resource intensive. So, the Poisson-equation method was chosen for the wall-distance computation based on good accuracy and computational time. The residual for the Poisson equation should be closely observed to determine the required number of iterations to obtain wall distance at a desired tolerance.

For the reported verification study, OpenFOAM computes solutions only for Test Case 1. For this specific problem, the HiSA (High Speed Aerodynamics) solver [103] is used, which was initially developed for compressible flow aerodynamics. The solver has the implementation of (Advection Upstream Splitting Method) AUSM$^+$-up [104] and HLLC [105] flux schemes. The implementation also has AUSM$^+$-up with a low-Mach correction but was observed to result in spurious pressure waves at the locations of skewed cells. The HLLC scheme was able to provide a much more accurate flow field. The GMRES method [31] accelerated the convergence. The pseudo-transient time discretization method is used with the HiSA solver. The Gauss-Green method is used to compute gradients, and a second-order accurate, linear upwind method [106] is used for the divergence terms.

IV. Test Case 1: Joukowski Airfoil

This 2D test case is designed as a relatively simple verification case for implementation of RANS equations where theoretically optimal convergence rates for drag coefficients can be observed. For adjoint-consistent discretization methods of nominal order $(P + 1)$, the optimal convergence rate of the error in the drag coefficient is expected to be $2P$. Without adjoint consistency, the drag-error convergence rate is expected to be at least $P + 1$.

A. Geometry, Flow Conditions and Grids

The Joukowski airfoil chosen for this test (Fig. 1) is a symmetric aerodynamic analytical shape that features a cusped trailing edge. A solution for a high-Reynolds-number flow at zero degrees angle of attack is expected to be smooth; however, there is a skin-friction singularity at the trailing edge. The flow conditions for this test case are the following: the freestream Mach number is $M_\infty = 0.15$, the Reynolds number is $Re_c = 6 \times 10^6$ based on the airfoil chord, the angle of attack is $\alpha = 0°$, and the reference temperature is $T_{ref} = 520 °R$. A no-slip adiabatic-wall boundary condition is set at the airfoil, and the far-field boundary conditions are based on an inviscid characteristic method.
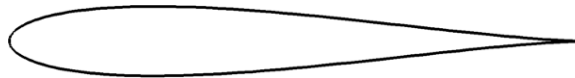

Fig. 1   Joukowski airfoil.

The family of fixed grids used in this study includes six nested, quadrilateral grids that follow the classic meshing guidelines requiring grid lines to be near orthogonal to the geometry and the sizes of neighboring elements to be similar. The grids are referenced as Grid 0 to Grid 6. The Joukowski conformal map is used to generate grids with nearly orthogonal grid lines. The coarsest Grid 0 is composed of 48×16 quadrilateral cells (48×17 grid points) in the chordwise and wall-normal directions, respectively; the finest Grid 6 grid is composed of 3072×1024 quadrilateral

cells (3072 × 1025 grid points). The grid statistics shown in Table 1 are for 2D grids. Finite-volume solvers often simulate 2D flows on 3D one-cell-wide grids; for such grids, the number of grid points doubles.

Table 1   Joukowski airfoil: statistics of fixed grids

Grid	Grid points (thousands)	Grid cells (thousands)
Grid 0	0.8	0.8
Grid 1	3.2	3.1
Grid 2	12.5	12.3
Grid 3	49.5	49.2
Grid 4	197.4	196.6
Grid 5	788.0	786.4
Grid 6	3145.7	3148.8

Three views of Grid 2 are shown in Fig. 2. The computational domain extends 100 chord lengths from the airfoil. The grids are stretched toward the viscous surface, toward the x-axis ($y = 0$) upstream and downstream of the airfoil, and toward the grid line that goes through the trailing edge and is orthogonal to the x-axis at the trailing edge. The wake grid opens as the mesh progresses aft of the airfoil trailing edge to reduce the maximum cell aspect ratio to approximately 100 near the outflow boundary. The grid clustering at the leading edge serves to capture the weak stagnation pressure singularity. The grid clustering at the trailing edge is needed to capture the skin-friction singularity. The grid spacing near the leading and trailing edges was repeatedly adjusted to produce grids that facilitate observation of expected error rates in the drag output with grid refinement. These geometry and grids have been used for verification of SA-neg-QCR2000 model [11] and for preliminary SA-neg-QCR2000-R solutions [18].

(a) Near surface view   (b) Wake view   (c) Global view
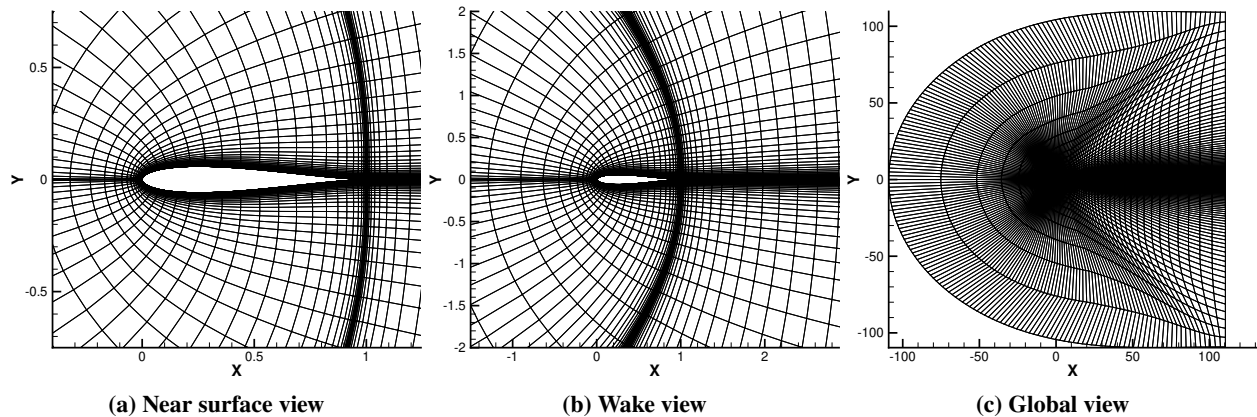
Fig. 2   Joukowski airfoil: Grid 2.

In addition, solution-adapted grids have been used by `SANS` and `WOLF`. `SANS` uses an the adjoint-based error estimator targeting reduction of the error in the drag coefficient. `WOLF` uses the *multiscale* error estimator minimizing the interpolation error.

`SANS` solutions use polynomials of degrees $P = 1$, 2, and 3, and provide nominal second-, third-, and fourth-order accuracy, respectively. The `SANS` formulation is adjoint consistent, thus the error in the drag coefficient is expected to converge with the second, fourth, and sixth order, respectively. All other solvers are formally second-order accurate and the corresponding error in the drag coefficient is expected to converge with second order. All solutions converged the root-mean-square (rms) norm of the residuals below 10^{-9} on all grids.

B. Grid Convergence

Nine sets of solutions were computed on the fixed grids and four sets of solutions were computed on families of adapted grids. Only CFD++ computed solution on Grid 6 in the family. Most of the solvers computed solutions on the six coarser fixed grids. Figure 3 shows a global view on the grid convergence of the total-drag coefficient and its pressure- and viscous-drag components. The horizontal dashed line indicates the presumed grid converged value. The drag coefficients are plotted versus a characteristic mesh size h = $(DOF)^{-1/2}$, where DOF are degrees of freedom associated with the grid—grid points for node-centered solvers and grid cells for cell-centered solvers. For USM3D-ME, CFD++, and OpenFOAM, DOF are 2D grid cells. For FUN3D, COFFE, WOLF, and SANS-P1, DOF are 2D grid points. Higher-order SANS solutions have more DOF on the same grids, reflecting the increased operation count in computing higher-order residuals. All drag coefficients converge very well in this global view. The viscous-drag coefficient shows little variation in grid refinement but makes a significantly higher contribution to the total drag than the pressure-drag coefficient.

Figure 4 shows a closeup view on the grid convergence of the drag coefficients. One observation is that higher-order solutions provide a better accuracy per degree of freedom than second-order solutions for all drag coefficients on fixed and adapted grids. Comparing solutions computed by the same solver on fixed and adapted grids, solutions on adapted grids provide significantly better accuracy per degree of freedom, as expected.

(a) Drag   (b) Pressure Drag   (c) Viscous Drag

Fig. 3   Joukowski airfoil: grid convergence of drag coefficient

(a) Drag   (b) Pressure Drag   (c) Viscous Drag
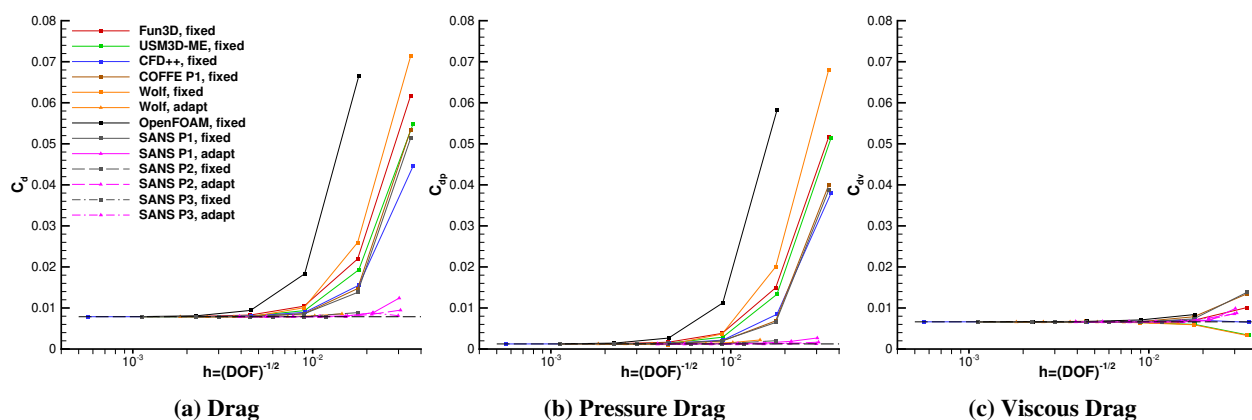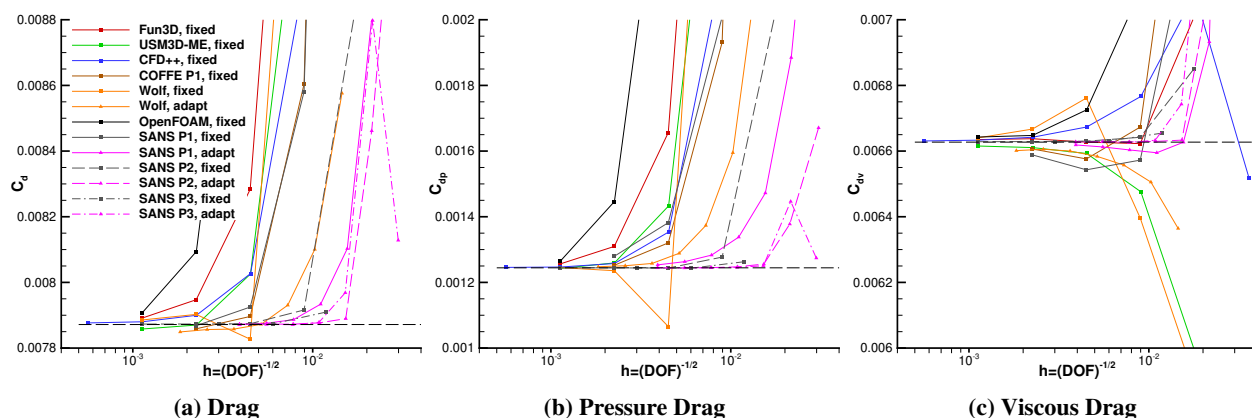
Fig. 4   Joukowski airfoil: closeup view on grid convergence of drag coefficient

Table 2 shows the absolute and relative variation between solutions computed on the finest grid in each set. The pressure-drag coefficient has the largest relative variation, but all curves shown in Fig. 4(b) keep getting closer to each other, so further reduction of the variation in the pressure-drag coefficient is expected with further grid refinement. The variation of the viscous-drag coefficient is small, but the tendency toward further grid convergence is less clear in Fig. 4(c). Several curves appear almost parallel to the horizontal line corresponding to the presumed grid-converged value, and the curve of the WOLF solution on adapted grids (orange curve with triangle symbol)trends away from the

presumed grid-converged value. This mismatch may indicate insufficient resolution of the skin-friction singularity at the trailing edge.

Table 2   Joukowski airfoil: variation of drag coefficients computed on finest grids

Coefficient	Absolute variation	Relative variation
C_d	$7.849091E\text{-}03 - 7.907418E\text{-}03$	0.74%
C_{dp}	$1.242691E\text{-}03 - 1.279594E\text{-}03$	2.93%
C_{dv}	$6.588418E\text{-}03 - 6.642744E\text{-}03$	0.82%

Figure 5 shows convergence of numerical errors in the drag coefficients. For the error estimate, the "truth" values for the coefficients of total drag, pressure drag, and viscous drag are taken as the corresponding coefficients computed from the SANS-P3 solution on the finest adapted grid. The error in a coefficient is estimated as the magnitude (absolute value) of the difference between the coefficient computed on a given grid and the "truth" value of the coefficient. Note that the uncertainty in the truth values is on the order of 10^{-5}; thus, all errors that appear comparable to or smaller than the uncertainty threshold are not reliable. Nevertheless, estimated errors are plotted for all solutions for completeness. The slopes that represent convergence of second, fourth, and sixth orders are also shown. Convergence of the errors in the total-drag coefficient shown in Fig. 5(a) is mostly monotonic for all solutions that have errors significantly greater than 10^{-5}. In Fig. 5(a), all second-order solvers show error convergence rates that appear to be better than the second-order rate; SANS-P1 and COFFE solutions approach the fourth-order rate of the error convergence. The high-order solutions and solutions on adapted grids show smaller errors and higher convergence rate than second-order solutions on fixed grids. This trend is observed for all drag coefficients. Convergence of errors in the pressure drag coefficient shown in Fig. 5(b) appears as more regular, probably indicating less uncertainty in the truth value. Errors in the second-order solutions on fixed grids converge with similar rates somewhat better than the second-order rate. Grid convergence of errors in the viscous-drag coefficient is shown in Fig. 5(c). The big dips in the SANS-P1 and COFFE solutions on fixed grids are caused by crossing the presumed grid converged value. Other second-order solutions on fixed grids converge with the second-order rate.
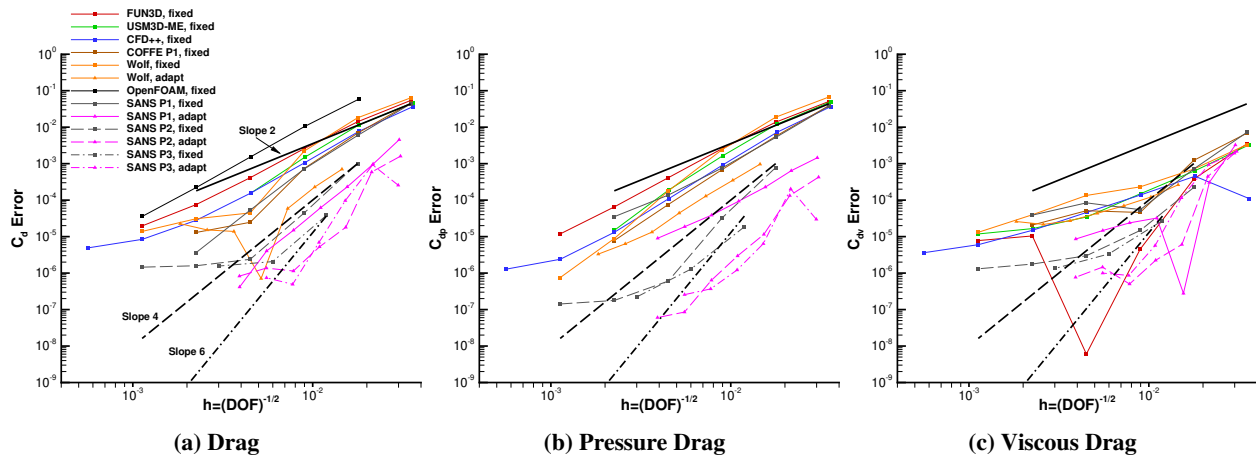

(a) Drag   (b) Pressure Drag   (c) Viscous Drag

Fig. 5   Joukowski airfoil: Grid convergence of drag coefficient numerical error

V. Test Case 2: Extruded NACA 0012 Wing in Tunnel

This test case is the main verification case for implementation of the SA-neg-QCR2000-R RANS equations. It is designed to observe and assess the effects of the rotation correction on the tip vortex. The case also features a juncture flow and highlights the QCR effects.

The original version of this case proposed in Ref. [18] included no-slip walls on all tunnel walls surrounding the wing, and the wing mounted at $10°$ angle of attack. However, as part of this collaborative effort, agreement on an asymptotic solution between the solvers was not obtained even with a grid resolution of 120 million points (330 million

cells). Since one of the goals of this effort is to obtain asymptotic solutions with a "reasonable" grid size, the case was simplified twice: first, by making all tunnel walls, except for the wing mount, as slip walls, and, second, by reducing the angle of attack to 5°.

A. Geometry, Flow and Boundary Conditions

The test case considers a subsonic flow around a 3D configuration that represents an NACA 0012 wing extruded from a wall of a tunnel with a rectangular cross-section. The model is similar to the one considered in Ref. [13]. The non-dimensional rectangular wing has a span of 0.75 and a constant cross-section in the shape of the NACA 0012 airfoil with a sharp trailing edge and unit chord. The wing has a rounded tip. The tunnel test section has unit width, height of $\frac{2}{3}$, and length of 3. The wing is mounted on the test-section wall corresponding to $y = 0$ with pitch angle of 5°; the opposite wall is located at $y = -1$. The quarter-chord location of the root airfoil corresponds to $x = 0$. The limits of the x and z coordinates of the tunnel test section are $-1 \leq x \leq 2$ and $-\frac{1}{3} \leq z \leq \frac{1}{3}$, respectively. Comparing to Ref. [13], the x range has been increased.

The inflow conditions are: Mach number $M = 0.2$, Reynolds number $Re = 4.6 \times 10^6$ based on the unit length, and angle of attack $\alpha = 0°$ with respect to the tunnel. The reference temperature is $T_{ref} = 521°$R. No-slip wall boundary conditions are assigned to the wing surface and the mounting wall of the tunnel test section. The other three walls of the test section and all extensions upstream and downstream of the test section have tangency-wall (perfect slip) boundary conditions. The upstream extension, $-2 \leq x \leq -1$, has the same rectangular cross-section as the test section. For meanflow, subsonic inflow boundary conditions are specified at $x = -2$, where the ratio of the total pressure to the reference pressure is set to 1.02828 (based on $M = 0.2$), the ratio of the total temperature to the reference temperature is set to 1.008, the flow angle is set to zero, and the velocity magnitude is extrapolated from the interior. The downstream tangency-wall extension section narrows over $2 \leq x \leq 6.5$ to a rectangular cross-section of width 0.9 and height 0.6 centered at $z = 0$. This converging section is needed to increase the flow speed and prevent reversed flow at the outflow boundary at $x = 6.5$, where the ratio of the back pressure to the reference pressure is set to 1.0 and all other solution quantities are extrapolated from the interior. The wall distance used in the turbulence model is computed from the closest wall, either no-slip wall or tangency wall. The turbulence variable is set to zero on all walls, to the freestream ratio at the inflow boundary, and extrapolated from the interior at the outflow boundary. Figure 6 shows a global view of the computational geometry and a view of the wing inside the tunnel test section. The cyan and grey colors indicate no-slip and tangency wall boundaries, respectively; the blue and red colors indicate the inflow and outflow boundaries, respectively. Figure 7 shows a solution Q-criterion isosurface colored by the vorticity magnitude contours. A strong tip vortex and geometrical features associated with corners and interfaces between surfaces with different boundary conditions are highlighted.
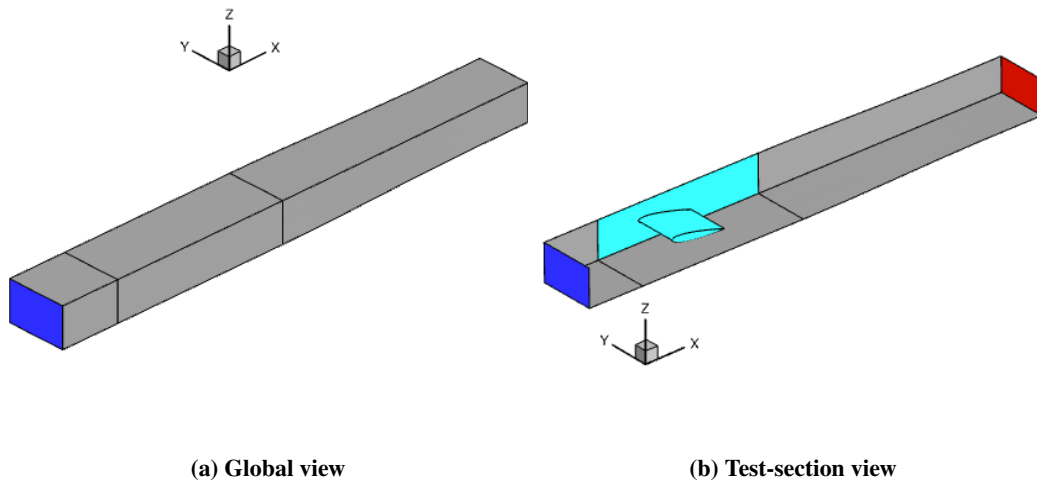

(a) Global view   (b) Test-section view

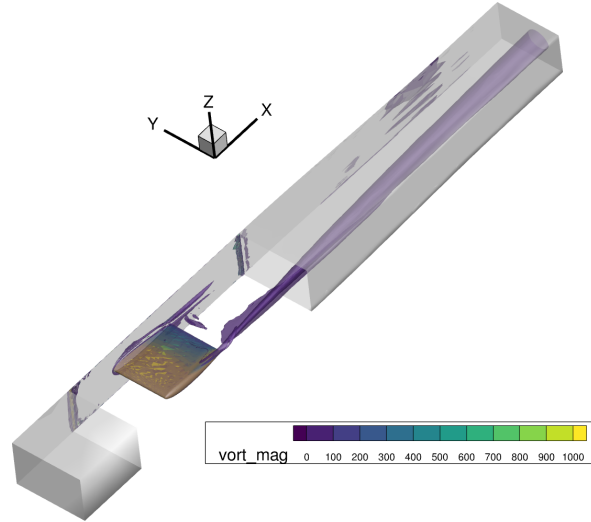**Fig. 6   NACA 0012 wing: geometry.**

14

Fig. 7   NACA 0012 wing: Q-criterion isosurface colored by vorticity magnitude.

B. Grids

Three families of grids have been shared for this study: two mixed-element grid families and a family of tetrahedral adapted grids. One family of mixed-element grids has been generated by `HeldenMesh`™ software [107] developed at Helden Aerospace, Inc. This family is referenced as the HM grid family. These grids were generated using an adaptive sourcing methodology in which a new mixed-element grid is generated using the Hessian of the local Mach number computed from an existing flow solution. One advantage of this approach is that it sets the local grid spacing and stretching ratios in order to accurately capture relevant flow features such as the wing-tip vortex and the wing-wake deficit, which propagate downstream toward the outflow. Other advantages are retaining prismatic and hexahedral elements within the boundary layer at the no-slip wall and a smoother variation in grid spacing. For this grid family, an initial best practice grid was generated on the geometry and a `USM3D-ME` solution was then computed at the prescribed flow conditions. The adaptive sourcing method was then used to generate Grid F. For Grid F, prismatic cells were generated near the wall corresponding to a first cell distance of $y^+ = 1$ (average) with approximately 30 layers within the boundary layer. All subsequent HM grids were then generated by scaling grid-spacing factors (including the boundary layer first cell height and growth rate) up or down to ensure a consistent grid family. The coarsest Grid C in the family has 80 thousand grid points and 275 thousand grid cells; the finest Grid Rb has 209 million grid points and 528 million grid cells. The three left columns in Table 3 show HM grid statistics.

The other mixed-element grid family has been generated by Cadence® software `Pointwise`™. This family is designated as the PW grid family. The PW grid family uses the Glyph script package GeomToMesh [108]. The grids are generated by a consistent refinement of the baseline grid that is tagged as Grid 1.0. The grid tag indicates the intended scaling factor of the grid edges. For example, edges of Grid 2.0 are intended to be two times shorter than edges of the baseline Grid 1.0. The grid generation process strictly follows the best practices in generation of grid families that provide user-specified resolution of all geometrical features and maintain smoothness of the surface and volume grids. The coarsest Grid 1.0 has 1.7 million grid points and 4.2 million grid cells; the finest Grid 4.0 has 63 million grid points and 173 million grid cells. The middle columns in Table 3 show PW grid statistics.

A series of adapted grids has been generated by MOESS. Total-drag error minimization in the `SANS` solutions is used as the goal for grid adaptation. The maximum of 40 grids has been set for each target DOF. From the series, six grids have been selected for the MOESS family of adapted grids. The grids are the optimal grids for the DOF count targeting 20K, 40K, 80K, 160K, 320K, and 640K grid points. The right columns of Table 3 show grid statistics of selected MOESS grids. Besides `SANS`, three other codes, `USM3D-ME`, `CFD++`, and `COFFE`, also compute solutions on the selected MOESS grids

In addition, two series of adapted grids were generated using `WOLF`, but these grids were not shared amongst the authors. The two series use *goal-oriented* minimization of errors in lift and drag, respectively, for the grid adaptation. A maximum of 20 adapted grids are generated for each target DOF. The exit criterion for each DOF is based on the relative difference, ϵ, between the aerodynamic coefficients computed on two subsequent adaptations. The relative

15

difference is set as $\epsilon = 1 \times 10^{-3}$ on coarse grids and progressively decreases to $\epsilon = 5 \times 10^{-5}$ with refinement.

Table 3   NACA 0012 wing: grid statistics (millions)

HM grid family			PW grid family			MOESS adapted grids		
Grid	Points	Cells	Grid	Points	Cells	Grid	Points	Cells
Grid C	0.08	0.27	Grid 1.0	1.71	4.22	Grid 20	0.02	0.10
Grid M	0.44	1.65	Grid 1.5	4.65	11.76	Grid 40	0.04	0.20
Grid F	3.49	13.45	Grid 2.0	9.76	25.24	Grid 80	0.07	0.40
Grid R	107.66	273.26	Grid 3.0	28.75	76.84	Grid 160	0.15	0.80
Grid Rb	208.59	528.37	Grid 4.0	63.43	173.50	Grid 320	0.29	1.60
						Grid 640	0.60	3.20

C. Iterative Convergence

Fifteen solution sets have been computed by five solvers (CFD++, COFFE, FUN3D, USM3D-ME, and WOLF) on the HM, PW, and adapted grid families generated by MOESS and WOLF. Figure 8 shows residual convergence versus normalized iterations. For iterations shown in the figure, the solution on each grid is initialized by the constant flow corresponding to the inflow conditions. Each code uses different stopping criteria. CFD++ computes dimensional solutions. FUN3D, USM3D-ME, WOLF, COFFE, and SANS solve non-dimensional equations, but use different reference quantities. In Fig. 8(a), FUN3D residual convergence is shown for the solutions computed on the PW and HM grid families. The red plots show convergence of the mass-conservation residual on each grid; the black plots show convergence of the turbulence-model residual. The FUN3D iterations stop when the rms norm of the turbulence-model residual has converged below 10^{-12}. In Fig. 8(b), USM3D-ME residuals are shown for solutions on the PW and HM fixed-grid families and on the adapted grids generated by MOESS. The meanflow residuals combining residuals of the mass, momentum, and energy conservation laws are shown by green lines and the turbulence-model residuals are presented by black lines. At least ten orders of residual reduction have been achieved on each grid. Figure 8(c) shows residuals of CFD++ solutions on the PW, HM, and MOESS grids. Blue lines represent the mass-conservation residuals and black lines represent the turbulence-model residuals. The CFD++ residuals appear elevated in comparison with the FUN3D and USM3D-ME residuals on the same grids because CFD++ solutions are dimensional. Between 3,800 and 10,000 iterations have been performed on each grid, and between seven and sixteen orders of residual reduction have been achieved. In Fig. 8(d), the mass-conservation and turbulence-model residuals of WOLF solutions are shown on the HM grids. Qualitatively, WOLF's residuals behave differently from the residuals of another node-centered, finite-volume code that solves nondimensional equations, FUN3D (see Fig. 8(a)). In particular, WOLF's mass-conservation residuals are significantly higher than the turbulence-model residuals, while FUN3D residuals exhibit the opposite trend. WOLF's nondimensionalization is different from that of FUN3D, thus the levels of residuals cannot be compared directly. Another difference is that WOLF reports the l_2-norm of residuals, while FUN3D reports the rms norm of residuals. WOLF's computations perform several initial first-order iterations to minimize transient effects in the solution; only target second-order residuals are shown on each grid. Residual reduction of at least four orders of magnitude has been achieved on each grid. In Fig. 8(e), plots show convergence of the mass-conservation residuals of the COFFE solutions on HM Grids C, M and F, PW Grids 1.0 and 1.5, and the MOESS adapted grids. The residuals are normalized by the initial residual. Ten orders of magnitude reduction is achieved on each grid. Although not shown in a figure, SANS solutions computed on the MOESS grids converge the rms norm of residuals below 5×10^{-9} on each grid. Similarly, WOLF solutions on adapted grids converge the l_2 norm of residuals below 1×10^{-8} on each grid.

(a) FUN3D solutions on PW and HM grids

(b) USM3D-ME solutions on PW, HM, and MOESS grids

(c) CFD++ solutions on PW, HM, and MOESS grids

(d) WOLF solutions on HM grids

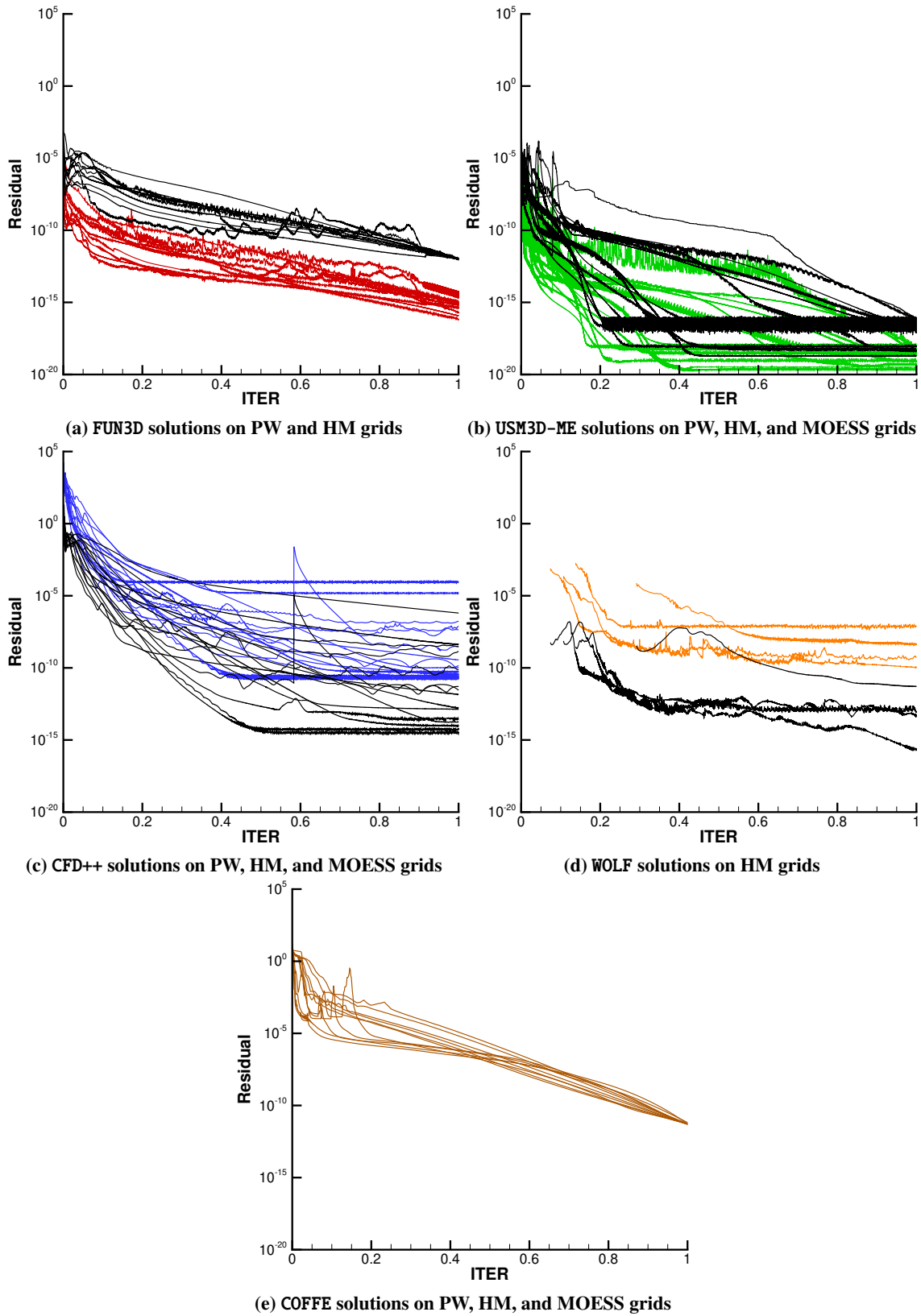(e) COFFE solutions on PW, HM, and MOESS grids

Fig. 8   NACA 0012 wing: residual convergence. Meanflow residuals are shown by color lines, turbulence-model residuals are shown by black lines.

D. Grid Convergence

Figure 9 shows grid convergence of the total-lift and total-drag coefficients as well as the pressure-drag and viscous-drag coefficients. The contributions to the total drag from pressure and skin friction are similar in magnitude and show similar variation in grid convergence. With the exception of WOLF solutions, the coefficients computed by different solvers on different grid families appear to converge to the same limits with grid refinement. WOLF solutions appear to converge to different values. The mismatch is most apparent on the HM grids where WOLF's lift and drag coefficients are clearly different from those approached by other solvers in grid refinement. The tendency is less clear on adapted grids. WOLF's lift coefficients computed on the adapted and HM grids agree to each other and disagree with other solvers. However, WOLF's drag coefficients computed on fine adapted grids are in a reasonable agreement with other solvers, especially on grids adapted for minimizing the drag error. Further investigation is needed to resolve this mismatch.

Considering convergence on the HM and PW families of expert-generated grids, all coefficients computed by CFD++, FUN3D, and USM3D-ME converge toward each other, indicating good grid convergence. COFFE computes solutions only on coarse grids from the HM and PW families. The total-lift coefficient computed by COFFE heads in the right direction, but still is far from the presumed grid-converged value indicated by other solvers; COFFE 's drag coefficients are in a good agreement with the coefficients computed by other solvers.

On adapted MOESS grids that use much fewer DOF than the PW and HM grids, SANS's total-lift and total-drag coefficients and COFFE's total-lift and pressure-drag coefficients show excellent agreement with the presumed grid-converged limits, indicating the superior accuracy per degree of freedom. SANS computes the total-lift and total-drag coefficients but does not provide drag components. COFFE's viscous-drag and total-drag coefficients show some change in the convergence trend on the finest MOESS Grid 640. CFD++ and USM3D-ME also compute solutions on the MOESS grids. The CFD++ coefficients trend in the right direction, but are not close enough to the presumed limits. The accuracy of the CFD++ coefficients computed on the MOESS grids is comparable with the accuracy of the coefficients computed on the PW and HM grids with similar DOF. An analogous trend is observed for the USM3D-ME lift coefficient. The USM3D-ME drag coefficients computed on MOESS grids seem to be closer to the presumed limits and exhibit better accuracy per degree of freedom than the USM3D-ME drag coefficients computed on the HM and PW grids with similar DOF. The viscous-drag and total-drag coefficients computed by all four solvers change the convergence trend on the finest MOESS grid, interrupting monotonic convergence. The change seems to be beneficial for accuracy of SANS's total-drag coefficient and CFD++'s viscous-drag and total-drag coefficients, but detrimental for accuracy of the total-drag and viscous-drag coefficients computed by COFFE and USM3D-ME. Convergence of the total-lift and pressure-drag coefficients appears to be less sensitive, although some changes in the lift-coefficient convergence pattern are visible in all solutions on the MOESS grids. Abrupt changes in the convergence trends may indicate insufficient convergence of the grid adaptation process and/or diminishing benefits of SANS driven grid adaptation for other solvers.
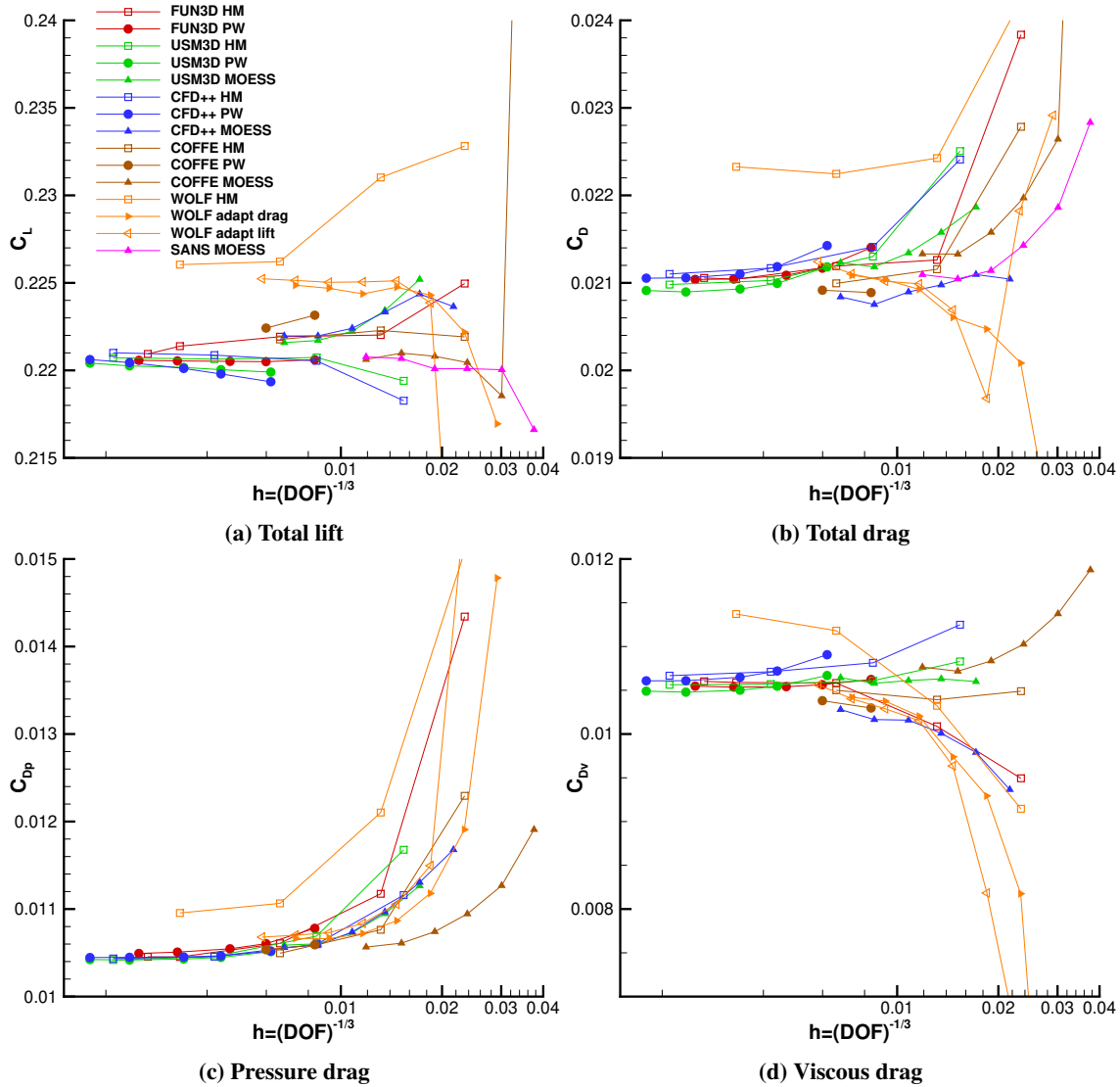
(a) **Total lift**

(b) **Total drag**

(c) **Pressure drag**

(d) **Viscous drag**

Fig. 9   NACA 0012 wing: grid convergence of lift and drag coefficients.

Table 4 shows variation of the lift and drag coefficients among the `FUN3D`, `USM3D-ME`, and `CFD++` solutions on the finest PW and HM grids and the `SANS` solutions for the total-lift and total-drag coefficients and the `COFFE` solutions for the total-lift and pressure-drag coefficients computed on the finest MOESS grid. The relative variation of the total-lift coefficient is less than 0.3%; the absolute variation in drag coefficients is less than 2 drag counts, and the relative variation is less than 1.7%.

Table 4   NACA 0012 wing: variation of lift and drag coefficients computed on finest grids with five solvers

Coefficient	Absolute variation	Relative variation
C_L	2.204141E-01 – 2.2103482E-01	0.28%
C_D	2.091254E-02 – 2.1096534E-02 (1.8 drag counts)	0.88%
C_{Dp}	1.041766E-02 – 1.0565747E-02 (1.5 drag counts)	1.41%
C_{Dv}	1.048994E-02 – 1.0662808E-02 (1.8 drag counts)	1.63%

19
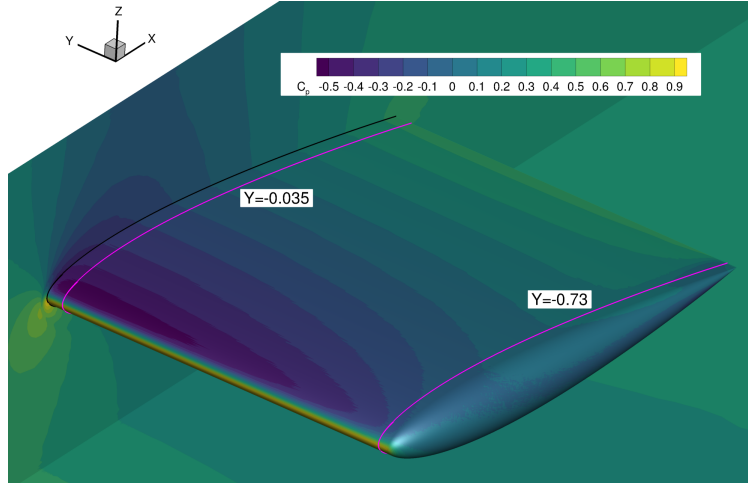
Fig. 10   NACA 0012 wing: locations of wing cross-sections.

E. Local Pressure and Skin Friction Profiles

In this section, variations of the surface pressure and skin friction are compared for solutions computed by different solvers on different grids. Two wing cross-sections are identified and illustrated in Fig. 10. The wing and wall surfaces in the figure are colored by contours of the pressure coefficients. Each wing cross-section corresponds to a cut by a plane that is defined by its y-coordinate and parallel to the xz-coordinate plane. The cross-section corresponding to $y = -0.035$ represents flow near the wing-wall juncture and the cross-section corresponding to $y = -0.73$ represents the wing-tip flow.

The convergence of section C_p and $C_{f,x}$ using the HM grids is shown in Figs. 11 and 12 respectively. The suction peak near the leading edge at $x = -0.035$ as well as the tip vortex suction peak near the trailing edge at $x = -0.73$ appear to be converged with the HM grid sequence. Similarly, the section $C_{f,x}$ also appears converged, except for the WOLF solutions which exhibit distinct oscillations. The section C_p at $x = -0.035$ using the PW grids, shown in Fig. 13, is well converged. However, the tip-vortex suction footprint is not fully converged with the PW grids. The same trend is observed in the PW grid sequence section $C_{f,x}$ shown in Fig. 14. As shown in Fig. 15, the section C_p is also converged, both at the wing-root and wing-tip, using the MOESS adapted grid sequence. However, the $C_{f,x}$ are significantly "noisier", as shown in Fig. 16. The SANS $C_{f,x}$ is particularly noisy, though this is the result of plotting the piecewise constant values across elements. Finally, the section C_p and $C_{f,x}$ computed using the sequence of grids generated using WOLF are shown in Fig. 17. Here, the wing-root appears well converged, and the tip-vortex footprint is nearly converged. The skin friction is less noisy than that generated with the MOESS grid (likely due to the metric smoothing used with Feflo.a).

Figure 18 presents global views of the pressure variation along the two cross-sections on the finest grid used with the respective solver. For the wing-root section, all solutions appear identical, except for the C_p computed with WOLF, which appears to have an overall shift in C_p. This shift is consistent with the apparent different convergence in C_L shown in Fig. 9. The tip-vortex suction footprint near the trailing edge of the $y = -0.73$ section does, however, show differences between the solutions. A closeup view of the tip-vortex suction is shown in Fig. 19, where the overlay of all solutions in Fig. 19a shows relatively large spread in peak suction. However, the solutions computed using the HM grid, shown in Fig. 19b, do show good agreement between all solvers (aside from WOLF). Similarly, there is also good agreement between the peak suction value using a PW grid, aside from the FUN3D result. Notably, the peak suction value obtained with the PW grid is lower in magnitude relative to the value obtained with the HM grid. The largest spread occurs with the adapted meshes, despite the observed convergence in C_p in Fig. 15. Some of this variation can be attributed to differences in the discretization between the solvers, though it also likely indicates a higher grid resolution is required to obtain the asymptotic solution.
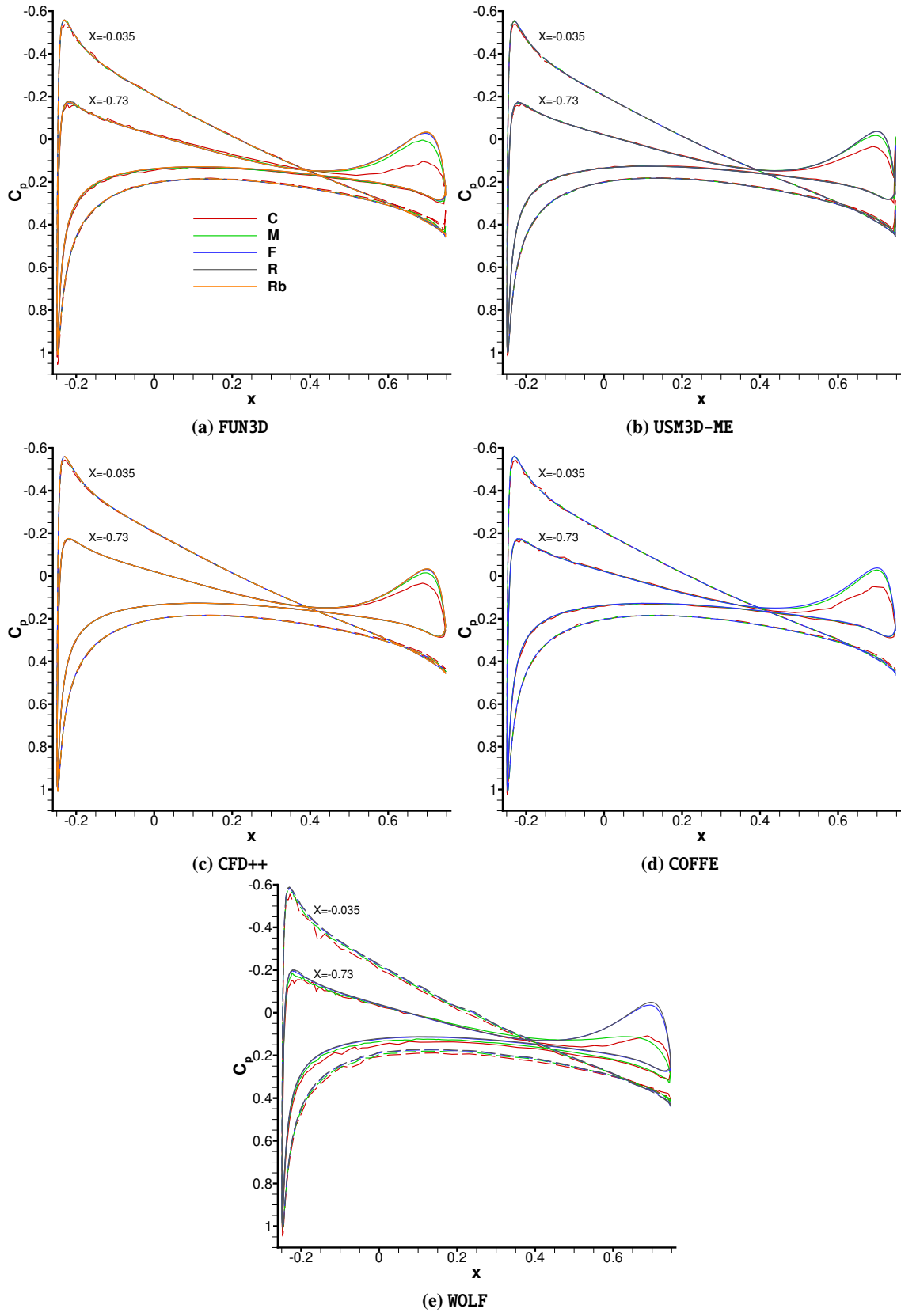
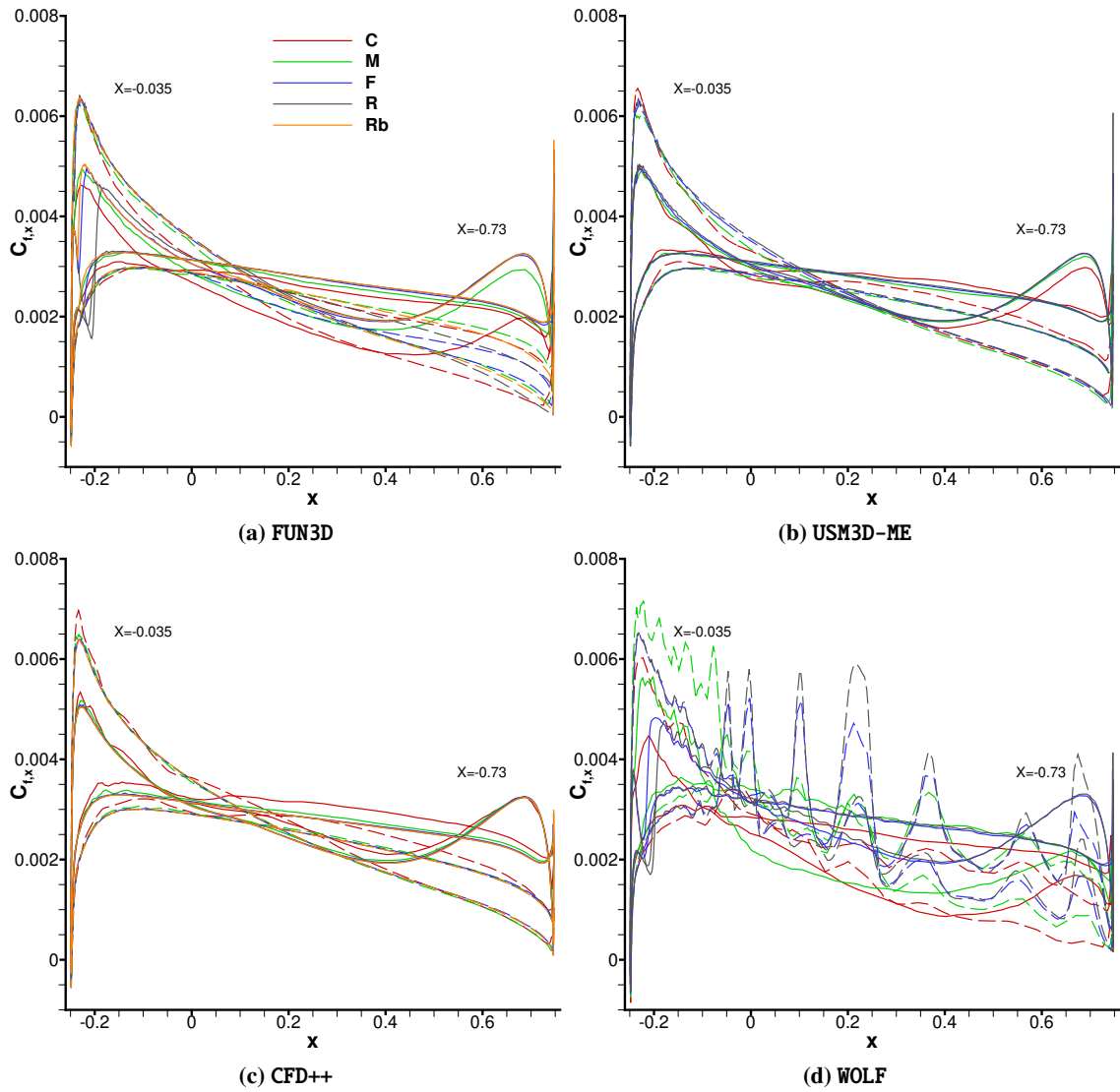**Fig. 11   NACA 0012 wing: Grid convergence of sectional pressure on HM grids.**

21

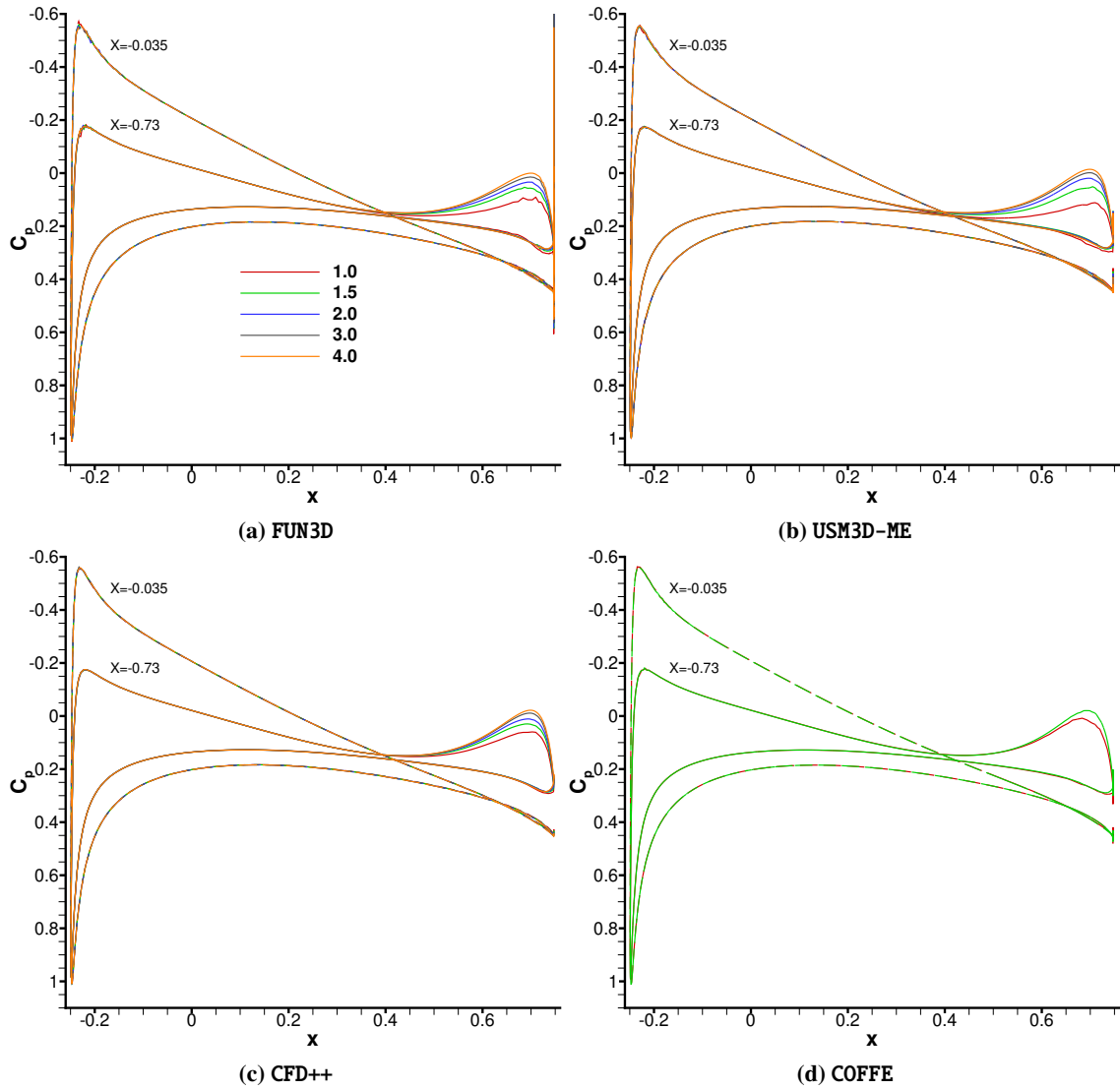**Fig. 12   NACA 0012 wing: Grid convergence of sectional skin friction on HM grids.**

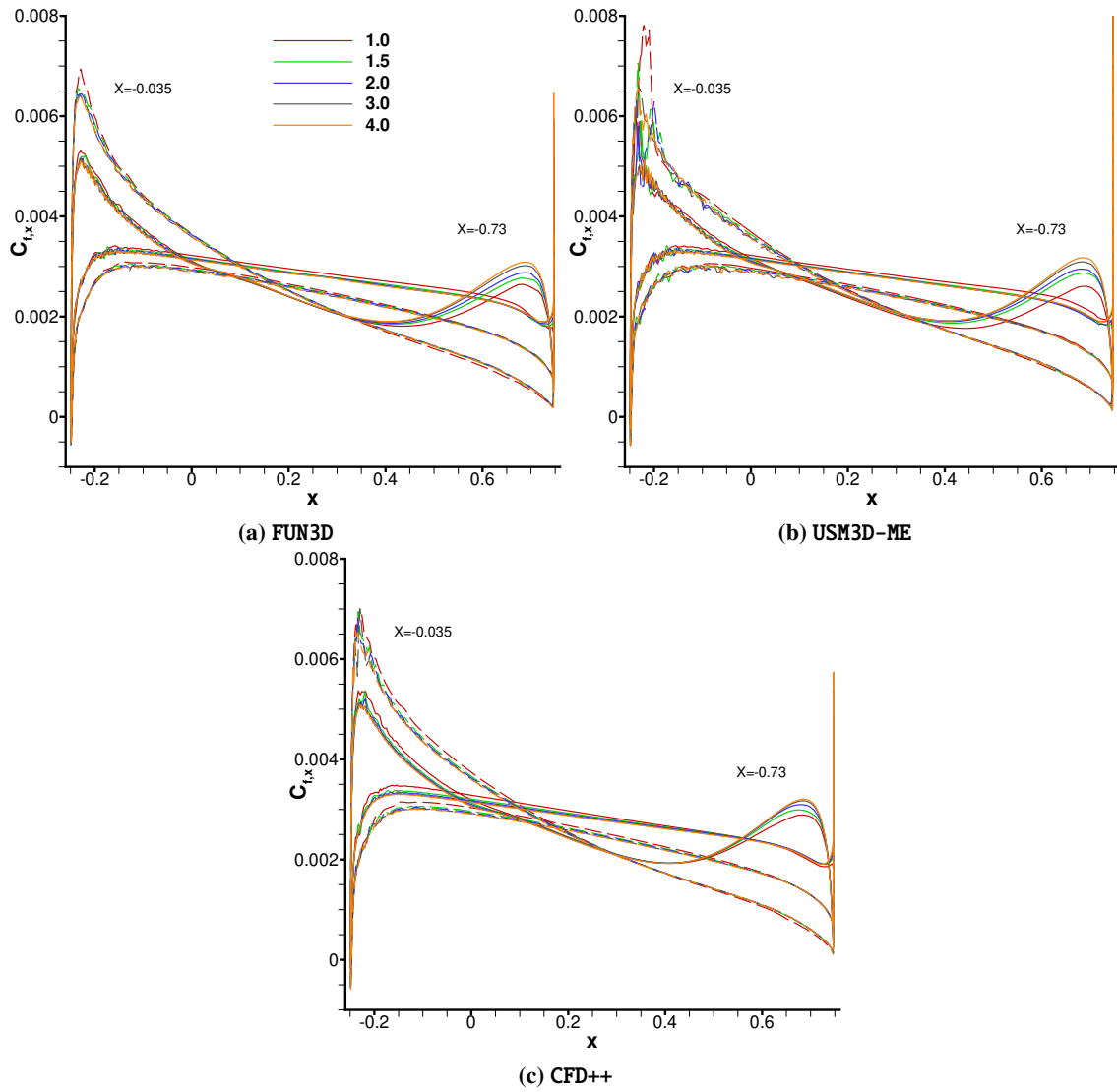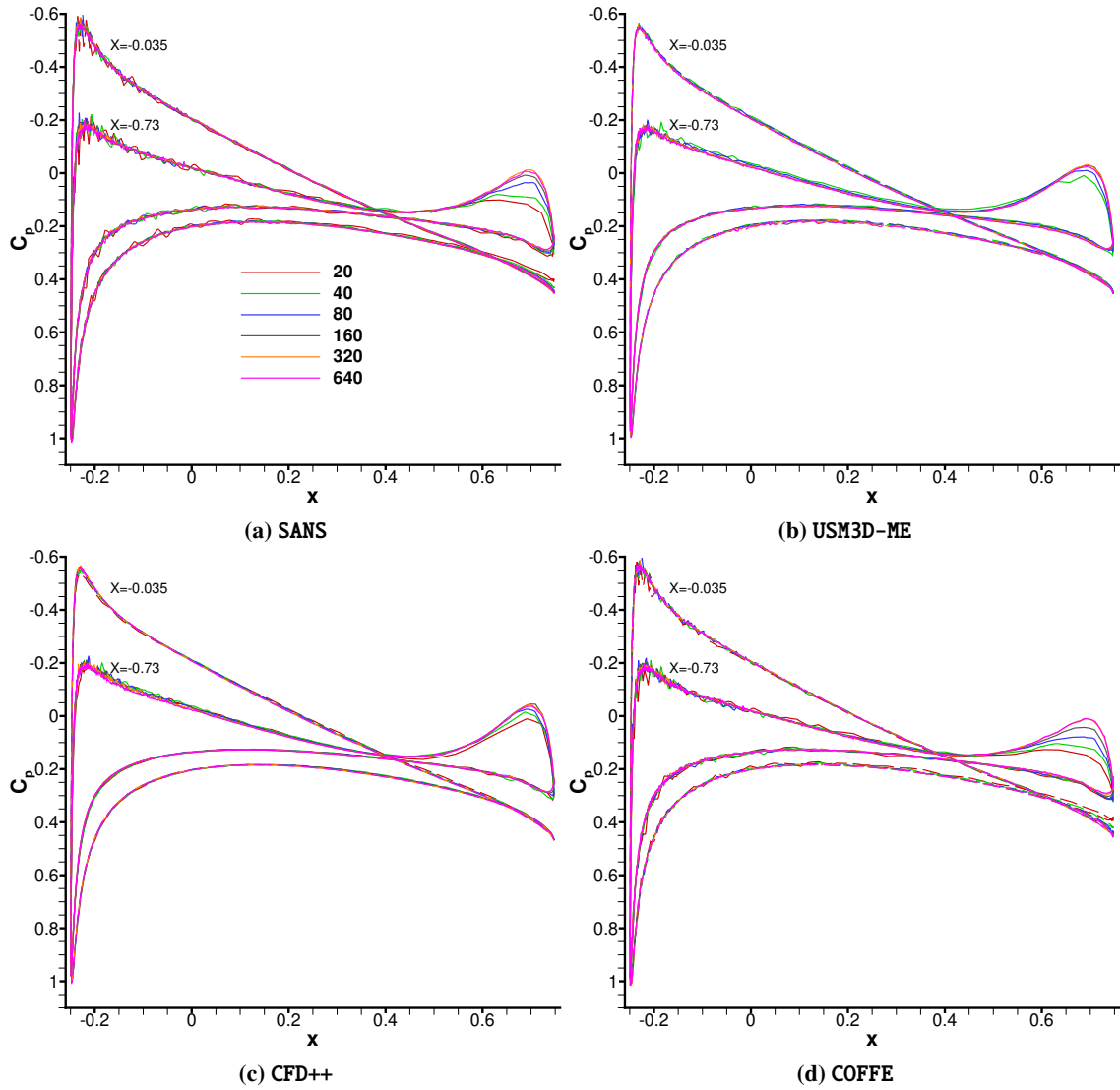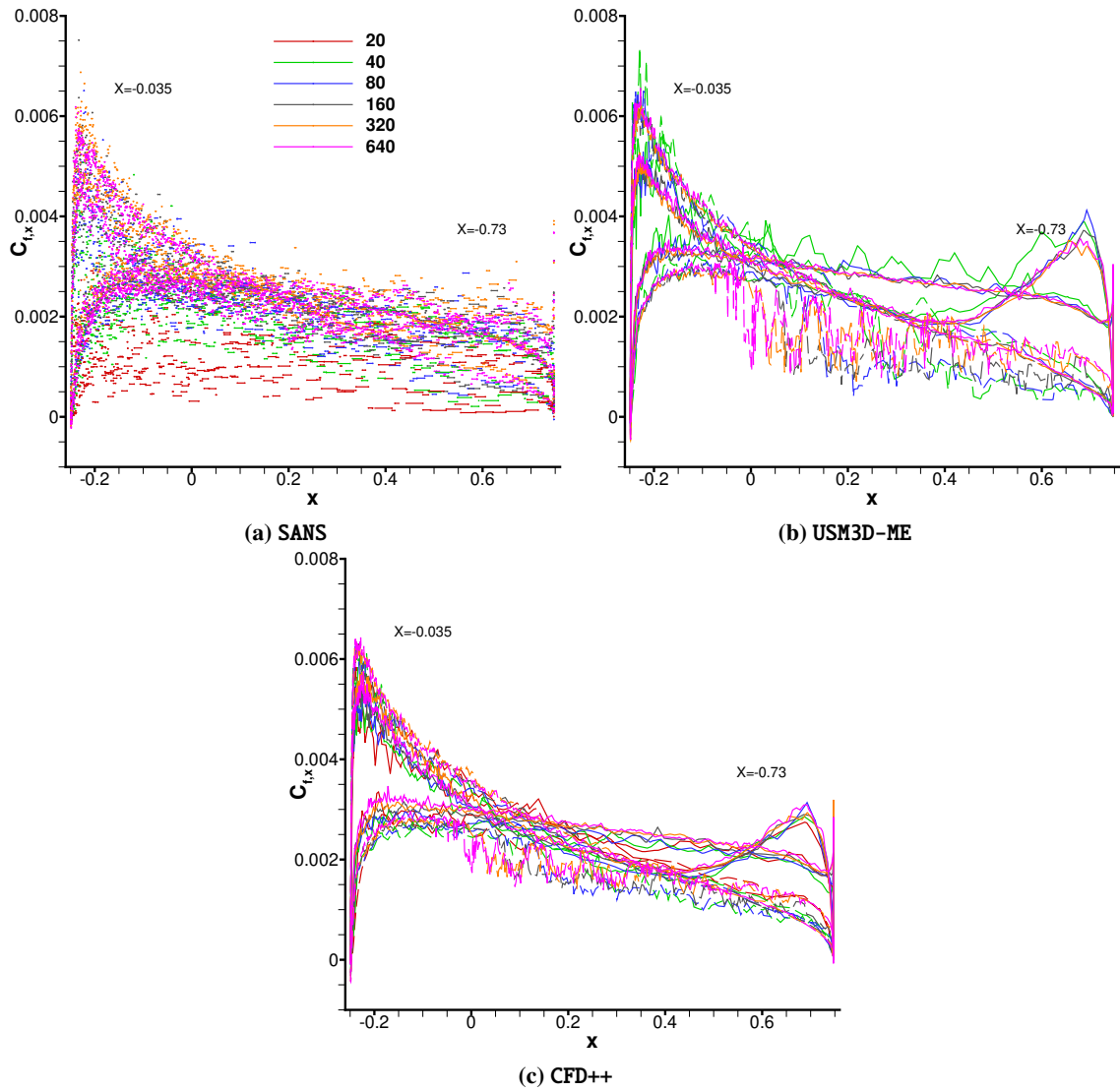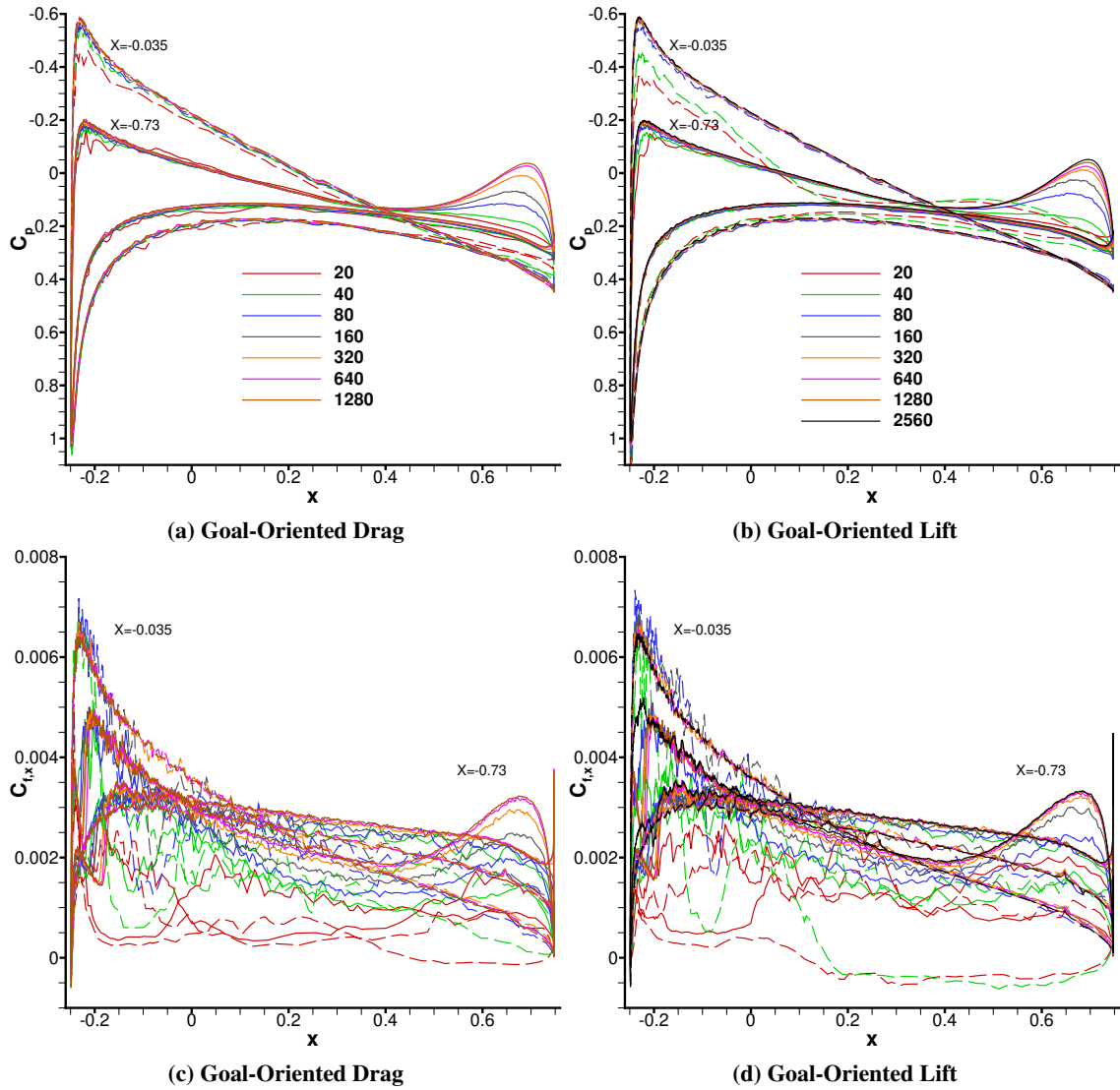**Fig. 13   NACA 0012 wing: Grid convergence of sectional pressure on PW grids.**

(a) FUN3D

(b) USM3D-ME

(c) CFD++

Fig. 14   NACA 0012 wing: Grid convergence of sectional skin friction on PW grids.

Fig. 15 NACA 0012 wing: Grid convergence of sectional pressure on MOESS grids.

Fig. 16 NACA 0012 wing: Grid convergence of sectional skin friction on MOESS grids.

(a) Goal-Oriented Drag

(b) Goal-Oriented Lift

(c) Goal-Oriented Drag

(d) Goal-Oriented Lift

Fig. 17   NACA 0012 wing: `WOLF` grid convergence of sectional pressure and skin friction on adapted grids with *goal-oriented* error estimate.

The global view of $C_{f,x}$ for the two sections is shown in Figure 20. Generally there is reasonable agreement between the solutions; however some of the solutions computed using adapted meshes and the `WOLF` solution computed using HM mesh are outliers. The exact cause of the large oscillations for the `WOLF` solution using the HM grid is not evident, it may be part of the solution, but is more likely a post-processing issue. More interestingly are some anomalies in the solution near the leading edge at the $y = -0.73$ section, which is highlighted in Fig. 21. Both the `FUN3D` solution and `WOLF` solution using the HM grid exhibit a "laminar-to-turbulent" transition with a sharp rise in $C_{f,x}$, as shown in Fig. 21b, however, since the SA model used here does not include a transition model, such an interpretation would be incorrect. Instead, this phenomena is more likely a result of excess dissipation from the discretization reducing the upstream value of χ, the f_{t2} activating only for the solvers, or simply an implementation "bug". Notably, both `FUN3D` and `WOLF` solutions follow the same $C_{f,x}$ values initially at the leading edge, but the $C_{f,x}$ rises sharply closer to the leading edge for `FUN3D`. This rise in $C_{f,x}$ is not observed in the PW solutions shown in Fig. 21c, but is also present for `WOLF` solution using the Goal-Oriented adaptation targeting drag shown in Fig. 21d.

(a) *y*=-0.035

(b) *y*=-0.73
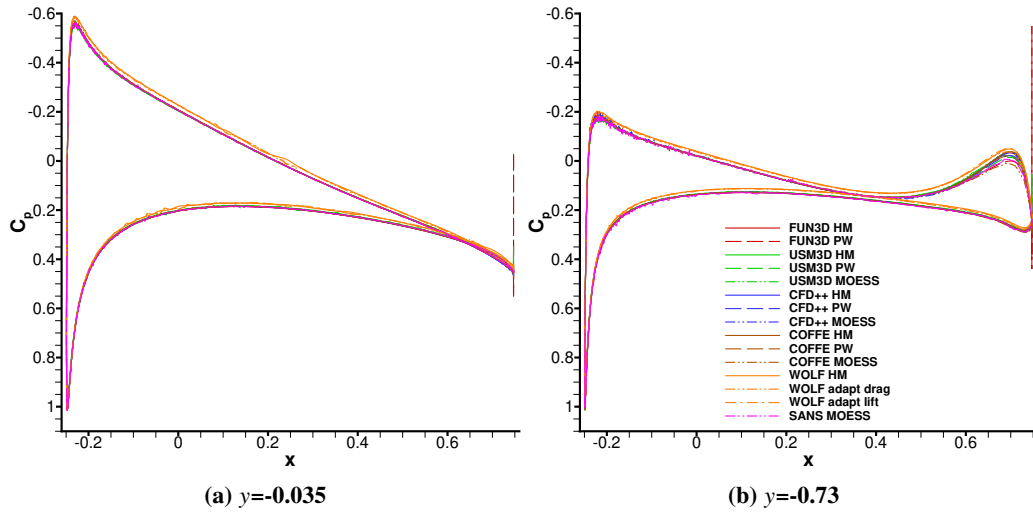
Fig. 18   NACA 0012 wing: finest grid global view on cross-section pressure coefficient.

(a) All grids

(b) HM grids

(c) PW grids

(d) Adapted grids
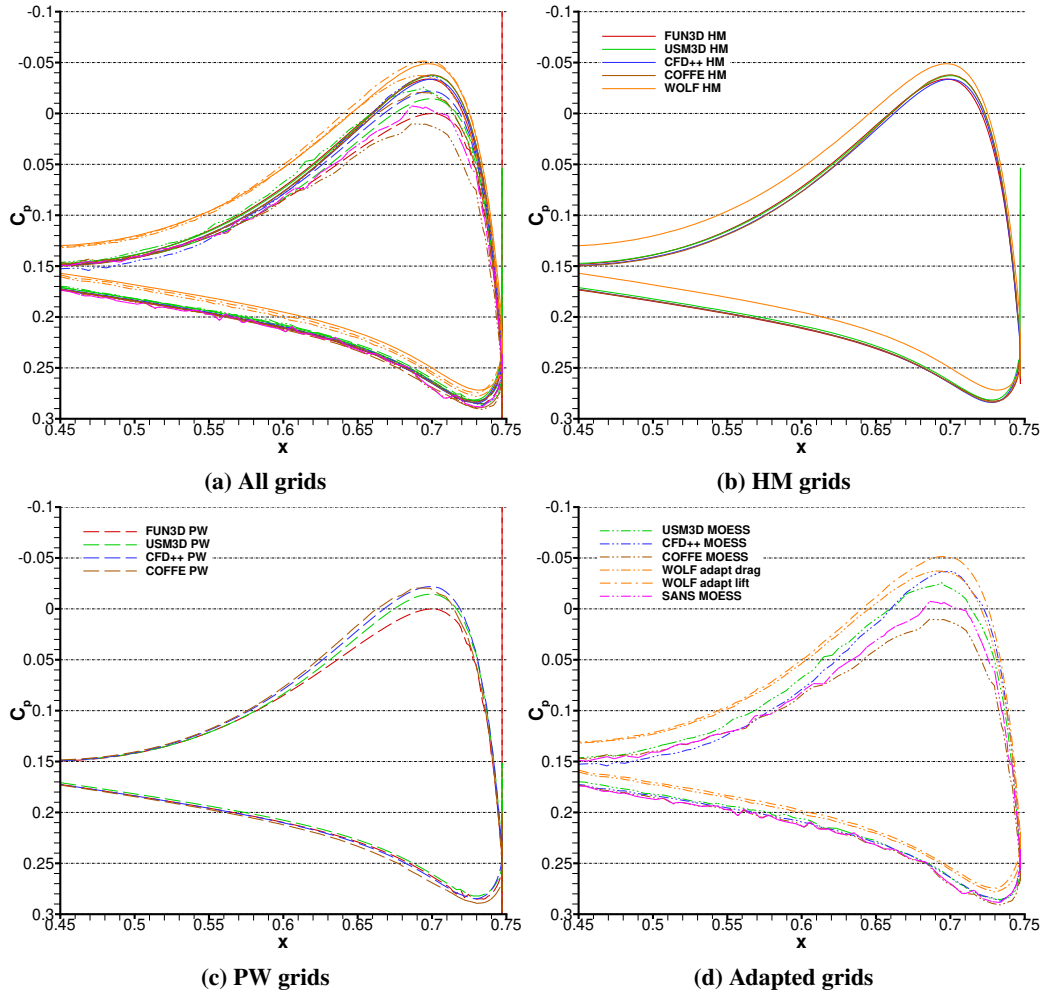
Fig. 19   NACA 0012 wing: zoomed view on *y*=-0.73 cross-section pressure coefficient near trailing edge.

(a) Y=-0.035

(b) Y=-0.73
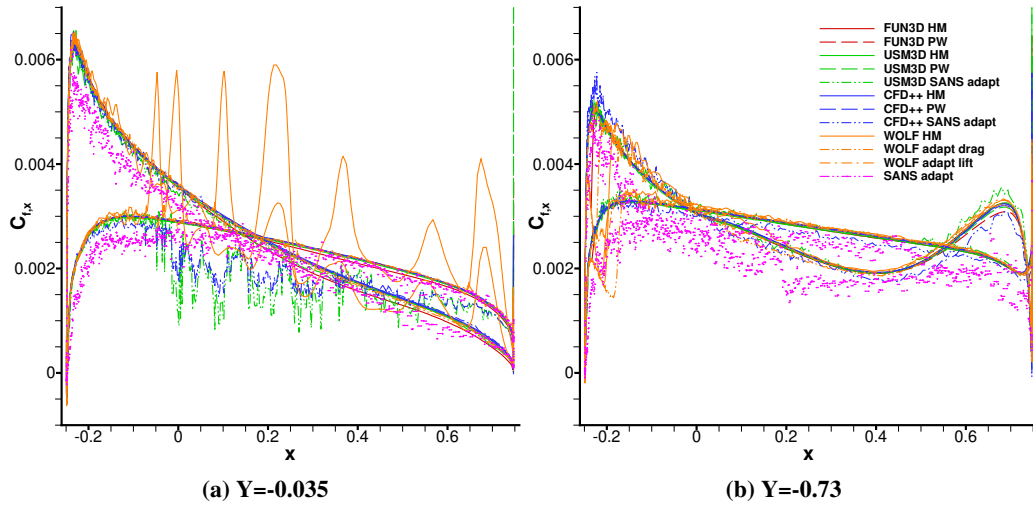
Fig. 20   NACA 0012 wing: x-component of section skin-friction coefficient.

(a) All grids

(b) HM

(c) PW

(d) Adapt
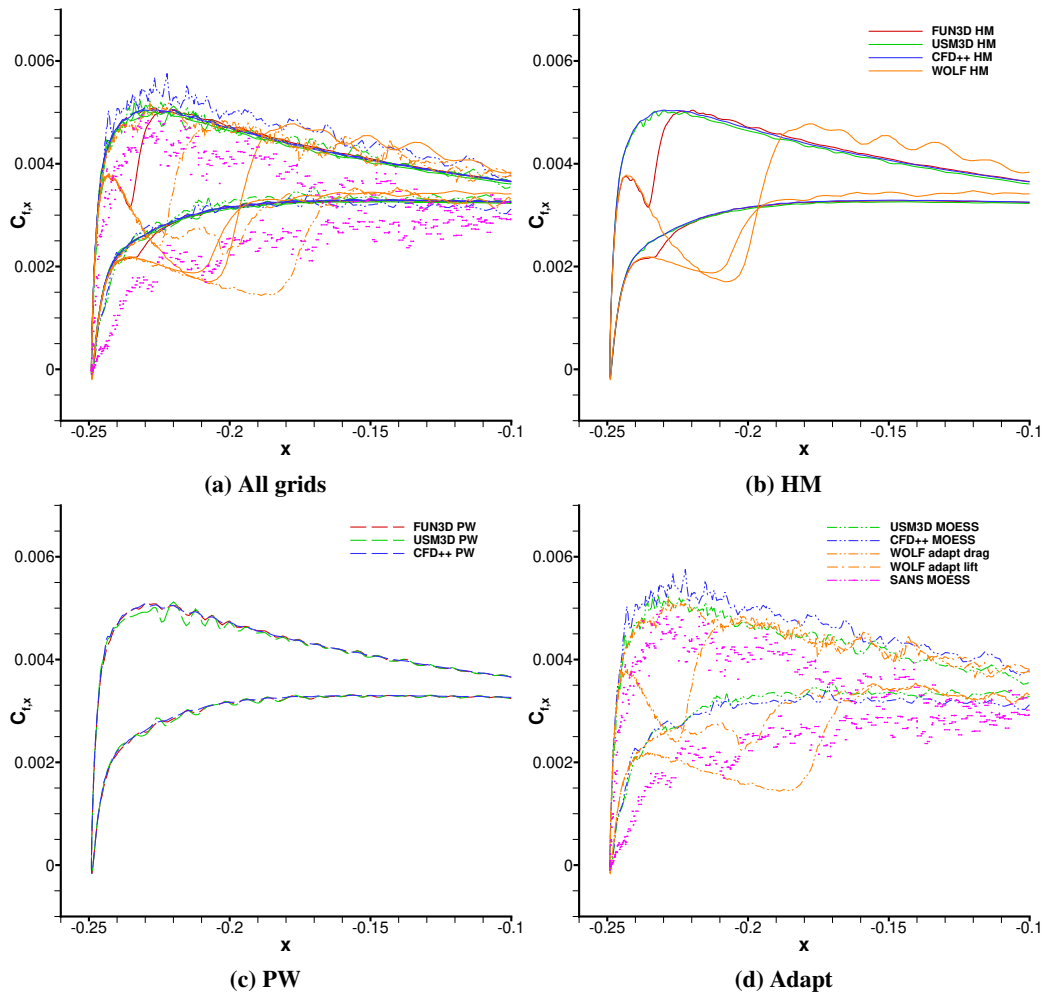
Fig. 21   NACA 0012 wing: zoomed view on on *y*=-0.73 cross-section x-component of skin-friction coefficient near leading-edge.

F. Effects of Rotation Correction

The main purpose of the rotation correction is to avoid spurious dissipation of free vortices caused by excessive eddy-viscosity generated by the SA and other turbulence models within a mature vortex. The mechanism to achieve this purpose is to minimize the production term of the SA turbulence model when the magnitude of the strain tensor (Eq. 25) is less than the vorticity magnitude (Eq. 14). To observe the expected effect, the contour levels of the turbulence working variable, $\hat{\nu}$, are monitored within two cross-sections of the tip vortex. The cross-sections correspond to planes parallel to the yz coordinate plane and characterized by the x-coordinate. One cross-section is located immediately behind the wing trailing edge and corresponds to $x = 0.8$. The second cross-section is placed downstream of the tunnel test section and corresponds to $x = 3.0$. Figure 22 illustrates the cross-sections and shows a global view of the observed contours of $\hat{\nu}$. Note that, in this global view, the $\hat{\nu}$ magnitude increases significantly downstream of the wing and still results in spurious vortex dissipation. This observation supports recommendations expressed in Refs. [13–15] to use the rotation correction with $c_{rot} = 2$ (Eq. 24) and allow negative production term in the SA model. The rotation correction considered in this paper uses $c_{rot} = 1$ and does not allow negative production.
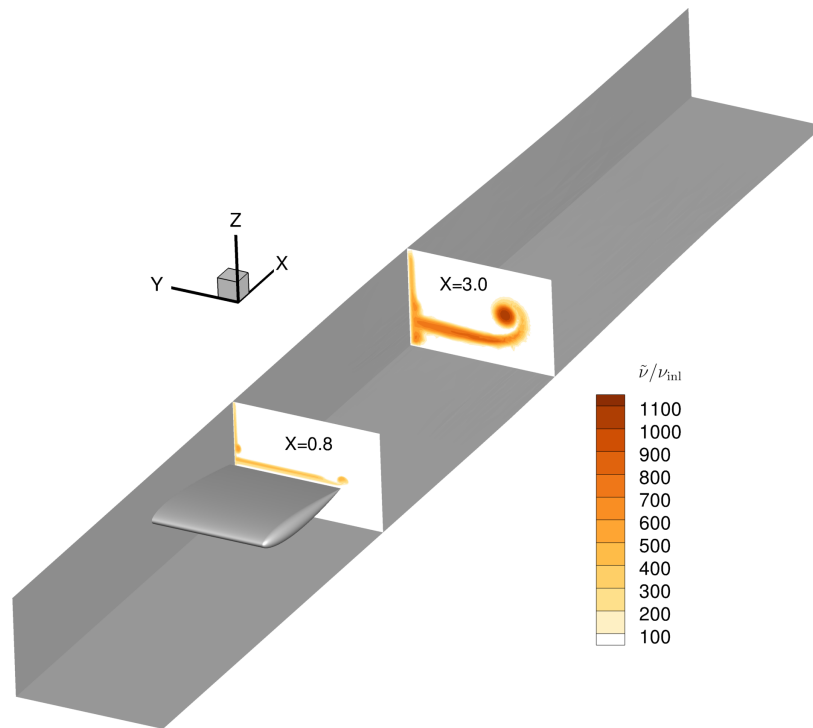

Fig. 22   NACA 0012 wing: locations of tip-vortex cross-sections.

Further in this section, we observe and assess the contours of $\hat{\nu}$ computed by different solvers on different grids. Figures 23 and 24 illustrate the effect of the rotation correction by comparing the SA-neg-QCR2000-R solutions computed by FUN3D, USM3D-ME, and COFFE on HM Grid F with the SA-neg-QCR2000 solutions computed by the same solvers on the same grid.

Figure 23 shows $\hat{\nu}$ contours in the cross-section corresponding to $x = 0.8$. The left and right figures in each row show contours corresponding to the SA-neg-QCR2000 and SA-neg-QCR2000-R solutions, respectively. Solutions computed with the same turbulence model by different solvers are hardly distinguishable in this view. Besides clear footprints of the trailed vorticity sheet (the narrow horizontal protuberance extending left from the mounting wall) and the tip vortex (the leftmost spot of the protuberance), the juncture vortices are also clearly seen near the mounting wall on the right. QCR is critical for correct representation of the juncture-flow vorticity. The main effect of the rotation correction is seen in a significant reduction of the $\hat{\nu}$ magnitude within the tip vortex observed in the right figure. All other flow features remain unchanged as expected.

Figure 24 shows $\hat{\nu}$ contours in the cross-section corresponding to $x = 3.0$. The magnitude and spread of the $\hat{\nu}$ contours have significantly increased in comparison those observed at the $x = 0.8$ cross-section. The major effect of the rotation correction is obvious: the strength and spread of the $\hat{\nu}$ contours is much greater in the left figures showing

solutions without rotation correction than in the right figures showing solutions with rotation correction. In the $x = 3.0$ cross-section, the $\hat{\nu}$ contours corresponding to the same model are significantly different. The differences are caused by variation in numerical dissipation produced by each solver on the same grid. The finite-element discretization by COFFE has lower numerical dissipation than a finite-volume discretization. USM3D-ME is a cell-centered solver that has more DOF on the same grid than FUN3D, a node-centered solver. Increased DOF count results in a reduced numerical dissipation. Somewhat counter-intuitive, SA-neg-QCR200-R solutions computed by less dissipative solvers result in higher levels of $\hat{\nu}$ and, as a result, higher turbulent eddy viscosity within the tip vortex.

(a) FUN3D, without R

(b) FUN3D, with R

(c) USM3D-ME, without R

(d) USM3D-ME, with R

(e) COFFE, without R

(f) COFFE, with R
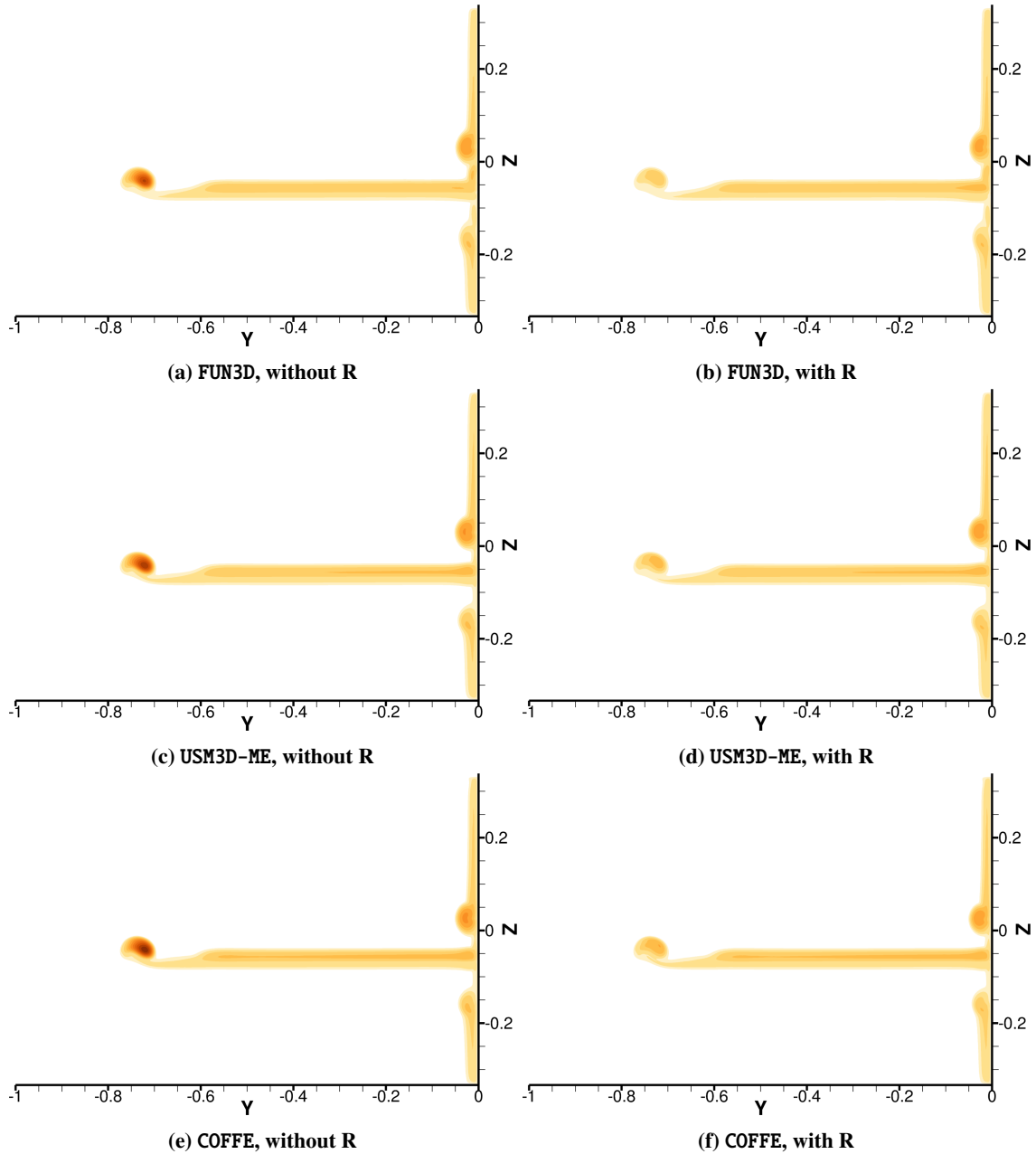
Fig. 23   NACA 0012 wing: effect of rotation correction on $\hat{\nu}$ contours on HM Grid F at cross-section $x = 0.8$ (color bar in Fig. 22).
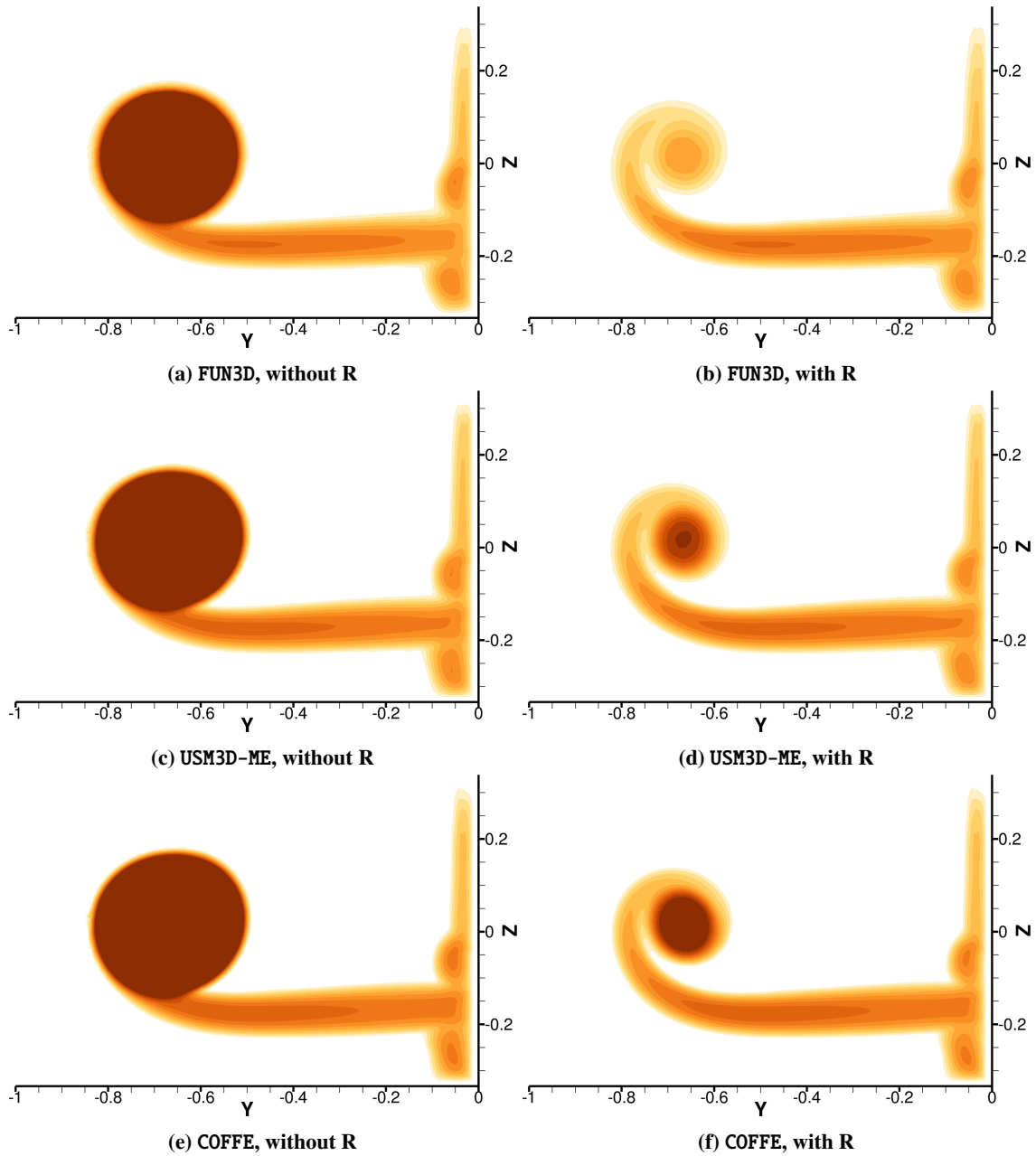
Fig. 24 **NACA 0012 wing: effect of rotation correction on $\hat{v}$ contours on HM Grid F at cross-section $x = 3.0$ (color bar in Fig. 22).**

An attempt to produce a grid converged representation of the $\hat{v}$ contours within the tip vortex has not succeeded. Downstream of the wing, the specific placement of degrees of freedom in each grid family strongly affects representation of the tip vortex. The resolution provided by the finest grids in each family is not sufficient to establish important features of the vortex. Nevertheless, within the $x = 0.8$ cross-section, the agreement between the $\hat{v}$ contours computed by different solvers on different grids is much better than the agreement within the $x = 3.0$ cross-section. Figure 25 shows the $x = 0.8$ cross-section of the finest grid in each family. The grids are qualitatively similar and provide increased resolution behind the wing trailing edge and especially behind the wing tip. MOESS Grid 640 uses visibly fewer DOF than other grids shown. Figure 26 shows the $\hat{v}$ contours within the $x = 0.8$ cross-section computed on the finest grids in each family. The contours are similar, although not identical; solutions on HM Grid Rb seem to generate the highest level of $\hat{v}$ within the tip vortex.
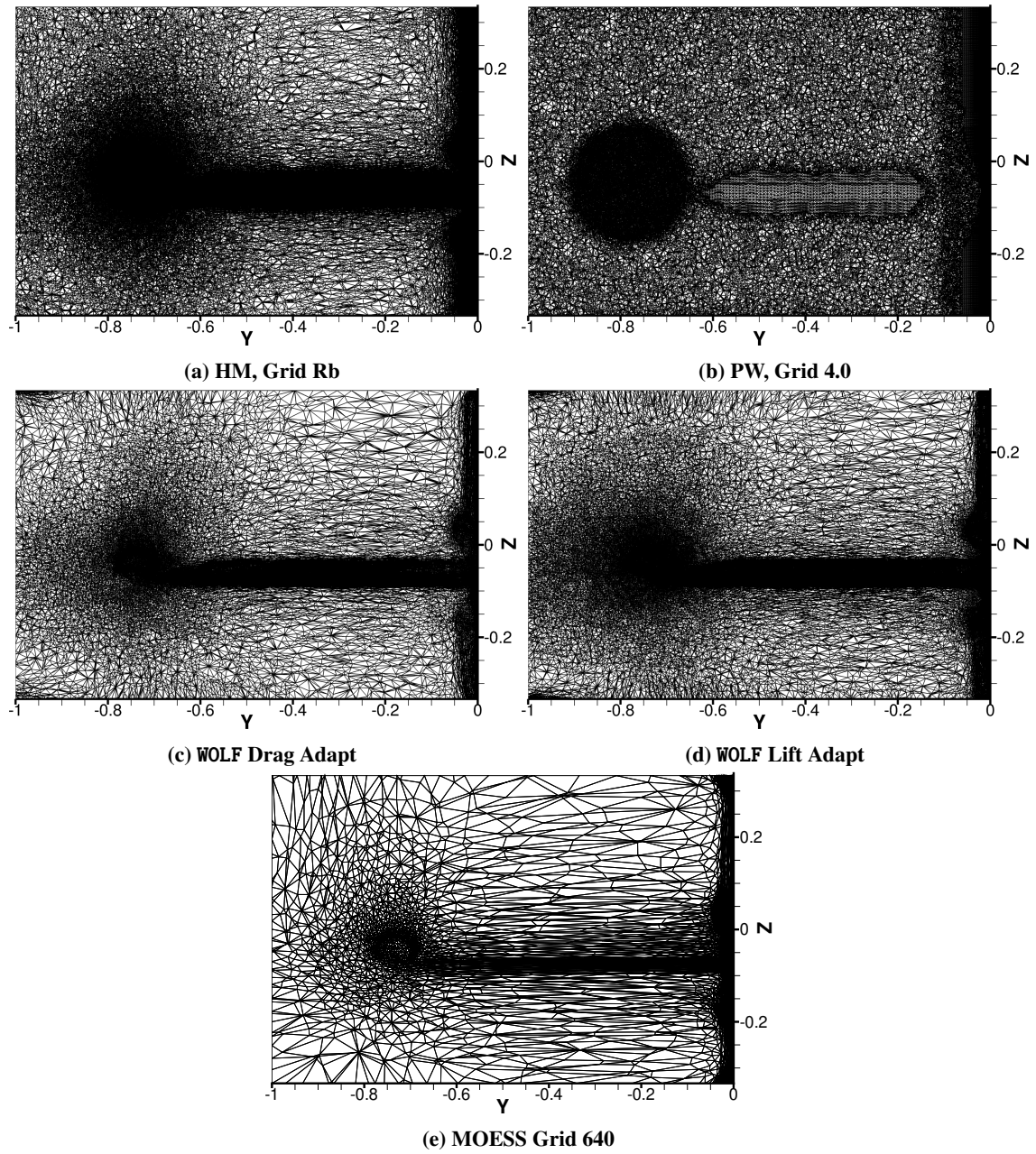
(a) HM, Grid Rb

(b) PW, Grid 4.0

(c) WOLF Drag Adapt

(d) WOLF Lift Adapt

(e) MOESS Grid 640

Fig. 25   NACA 0012 wing: $x = 0.8$ cross-section of finest grids in each family.

(a) FUN3D, HM Grid Rb

(b) CFD++, HM Grid Rb

(c) FUN3D, PW Grid 4.0

(d) CFD++, PW Grid 4.0

(e) WOLF Drag Adapt

(f) WOLF Lift Adapt

(g) SANS MOESS Grid 640

(h) COFFE MOESS Grid 640
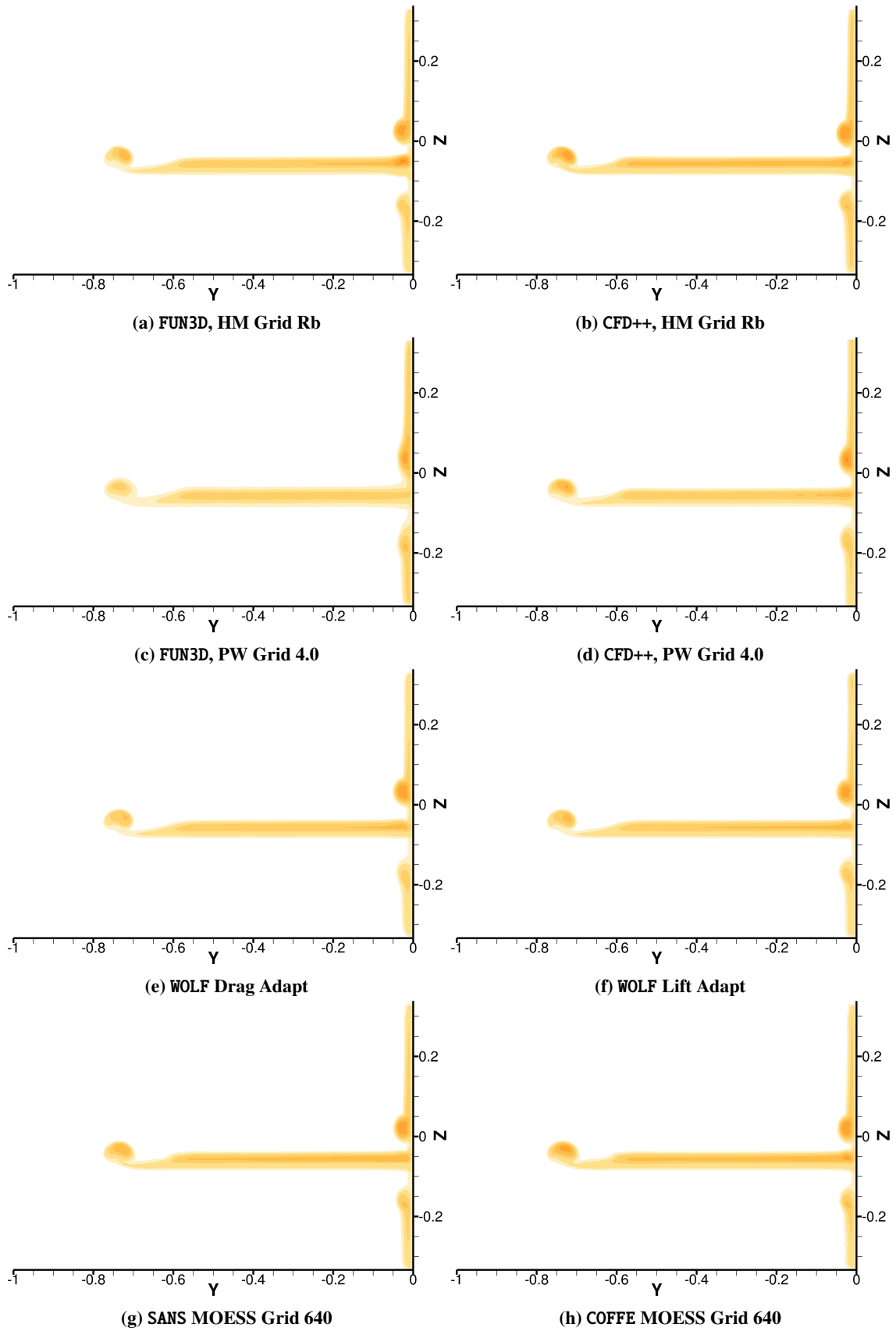
Fig. 26   NACA 0012 wing: $\hat{v}$ contours at cross-section $x = 0.8$ on finest grids in each family (color bar in Fig. 22).
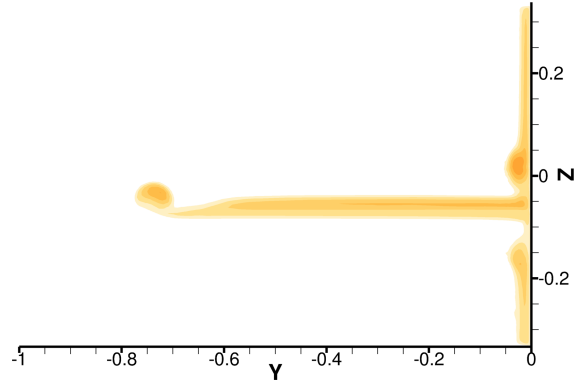
(i) CFD++ MOESS Grid 640

Fig. 26   Concluded.

The $x = 3.0$ cross-section of the finest grids in each family is shown in Fig. 27. The grids are significantly different. HM Grid Rb extensively refines the area near the wall and at the expected intersection with the tip vortex and the vorticity sheet. Recall that at this cross-section, the wall boundary condition is tangency wall. PW Grid 4.0 provides a near-wall refinement and uniform grid spacing away from the wall. WOLF adapted grids provide some additional refinement in the vortex/vorticity sheet area but use much coarser resolution near the wall. MOESS Grid 640 provides much coarser resolution everywhere but still clusters degrees of freedom near the wall and near the vortex. The $\hat{\nu}$ contours computed on these grids, shown in Fig. 28, are also very different. The tip vortex in the FUN3D solution on PW Grid 4.0 has been dissipated before reaching the $x = 3.0$ cross-section. The CFD++ solutions show a high level of $\hat{\nu}$ within the vortex core on the HM, PW, and MOESS grids. This performance may be attributed to the low-Mach-number preconditioning used in all CFD++ solutions computed for this paper. The shape and intensity of the $\hat{\nu}$ contours appear to be highly dependent on specific solver/grid combination. The $\hat{\nu}$ contours are smooth on the HM, PW, and WOLF adapted grids and irregular on the MOESS grid, although SANS and COFFE solutions on the MOESS grid are most similar to each other.
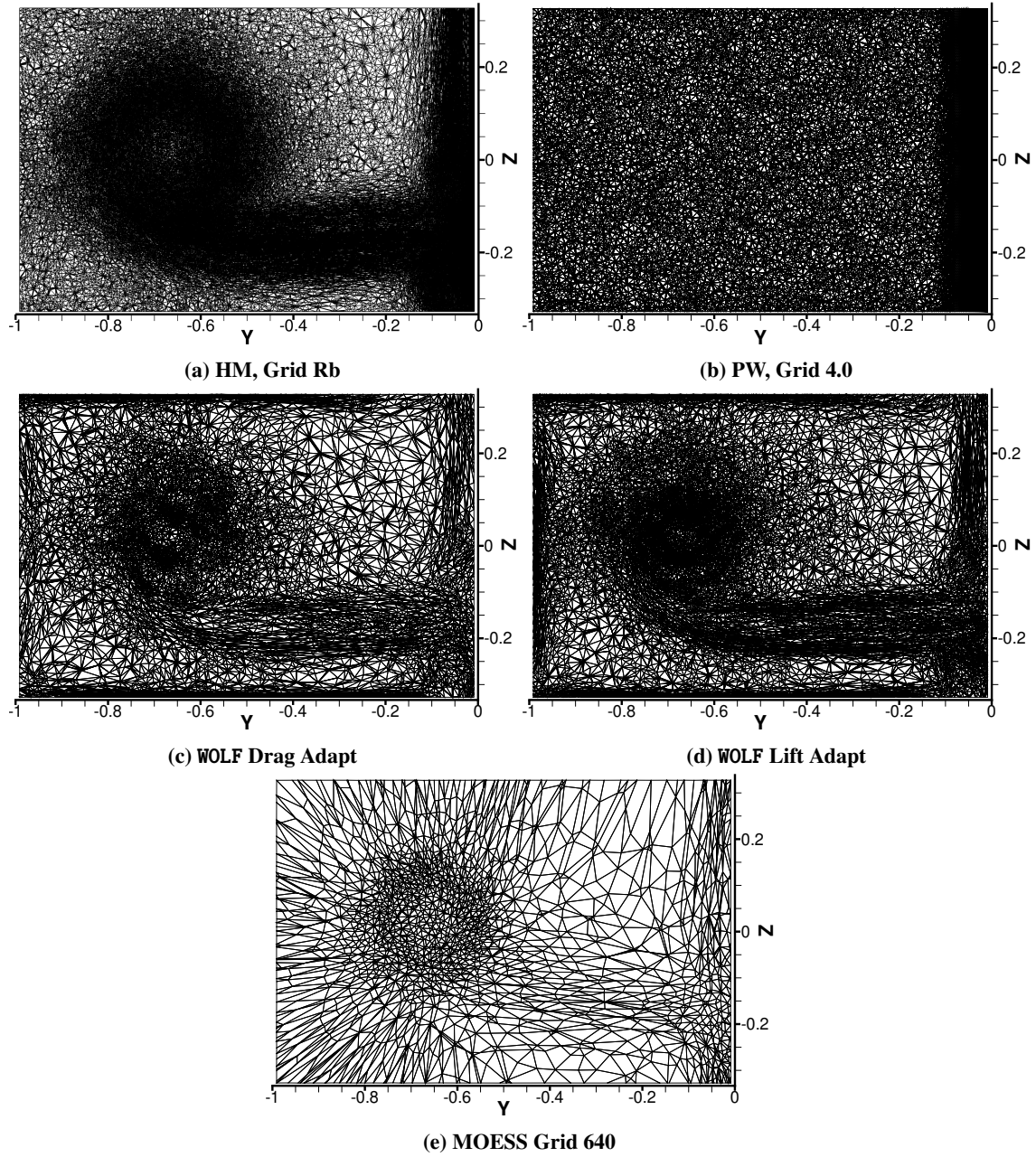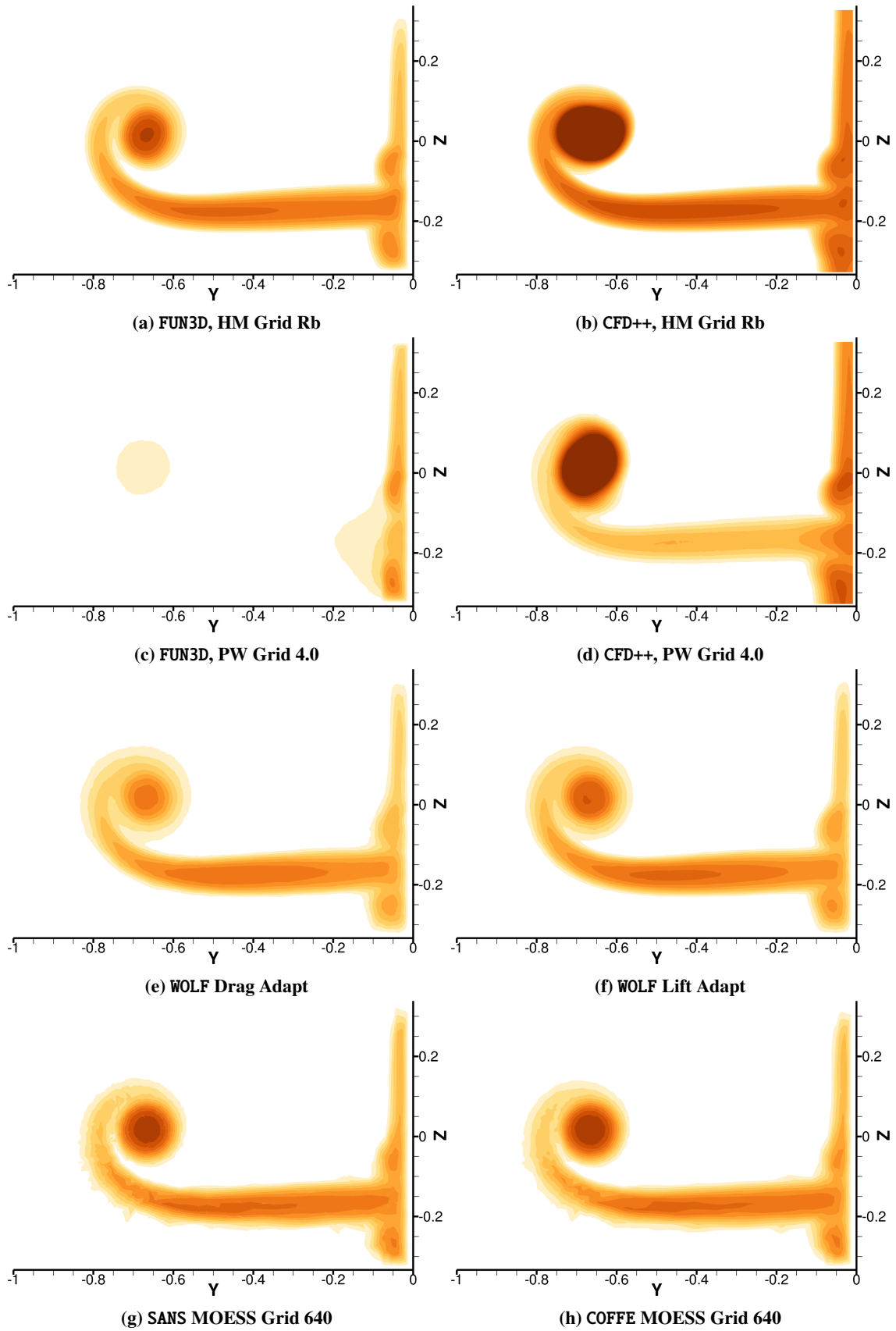
(a) HM, Grid Rb

(b) PW, Grid 4.0

(c) WOLF Drag Adapt

(d) WOLF Lift Adapt

(e) MOESS Grid 640

Fig. 27   NACA 0012 wing: $x = 3.0$ cross-section of finest grids in each family.

(a) FUN3D, HM Grid Rb

(b) CFD++, HM Grid Rb

(c) FUN3D, PW Grid 4.0

(d) CFD++, PW Grid 4.0

(e) WOLF Drag Adapt

(f) WOLF Lift Adapt

(g) SANS MOESS Grid 640

(h) COFFE MOESS Grid 640

Fig. 28   NACA 0012 wing: $\hat{\nu}$ contours at cross-section $x = 3.0$ on finest grids in each family (color bar in Fig. 22).
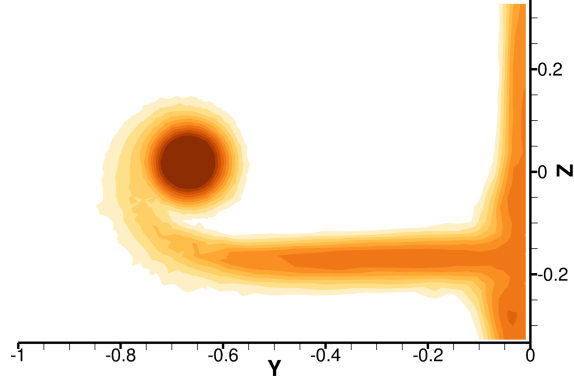
(i) CFD++ MOESS Grid 640

Fig. 28   Concluded.

VI. Test Case 3: High-Lift Wing-Body Common Research Model

A. Geometry, Flow, Boundary Conditions, and Grids

This test case is a common verification case with HLPW-5 [16]. The case considers a semispan wing-body configuration based on the family of standard high-lift geometries designed for studying aerodynamic phenomena associated with high-lift flow regimes. The configuration is designated as CRM-HL-WB. The original high-lift common research model (CRM-HL) [109] is an open-source, publicly-available commercial transport aircraft geometry in a high-lift configuration. The CRM-HL model is a complex configuration that features fuselage, wing, nacelle, pylon, leading-edge slats with under-slat wings, trailing-edge flaps, horizontal tail, main landing gear, and aileron. The CRM-HL-WB model considered here is a simplified version of the CRM-HL model that is designed for verification of solvers participating in HLPW-5. The CRM-HL-WB model has the fuselage and stowed wing geometry of the CRM-HL model with no other geometric features or bracketry. The model has a wing semispan of 1156.75 inches. The wing has a thin blunt trailing edge and a rounded tip cap. The mean aerodynamic chord (MAC) is 275.8 inches. The reference area is $297,360.0$ in^2. The entire computational domain is a rectangular cuboid with dimensions $-65,000 \le x \le 65,000; 0 \le y \le 65,000; -65,000 \le z \le 65,000$. The computational domain and the CRM-HL-WB geometry are illustrated in Fig. 29; representative streamlines and pressure-coefficient contours are shown on the surface.

The freestream flow conditions are Mach number $M = 0.2$, Reynolds number $Re_{\mathrm{MAC}} = 5.6 \times 10^6$, and angle of attack $\alpha = 11°$. The reference temperature is $T_{ref} = 521$ °R. The no-slip boundary condition is assigned to the wing and fuselage surface. Symmetry is specified at the $y = 0$ plane. The farfield boundary conditions based on Riemann invariants are assigned at all other boundaries of the computational domain. For the current verification studies, the target characteristics are grid convergence of the lift, drag, and pitching moment coefficients.
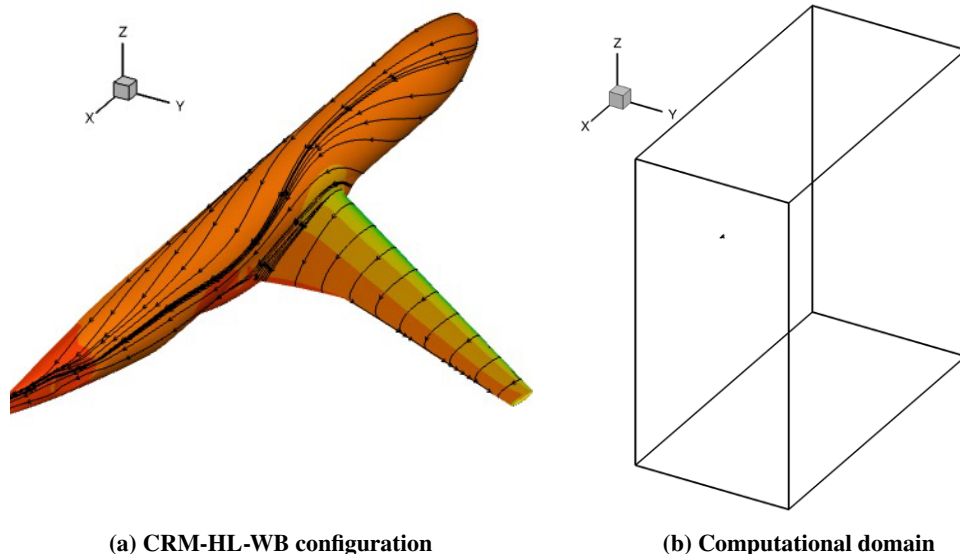
| (a) CRM-HL-WB configuration | (b) Computational domain |

Fig. 29   CRM-HL-WB model and computational domain for verification of high-lift flow solvers

Multiple grid families have been generated for the CRM-HL-WB and offered to the workshop participants through the HLPW-5 website [16]. The grids include nine families of mixed-element, tetrahedral, and hex-dominated grids generated for RANS solutions, four families of high-order grids, a family of adapted grids, and two grid families for large-eddy simulations (LES), from which one family is a hex-dominated grid family generated for hybrid RANS-LES and another family is a mixed-element grid family generated for wall-modeled LES. The intensive verification studies conducted by HLPW-5 participants conclusively showed that a satisfactory grid convergence and agreement between solutions computed by different solvers can be achieved on grids that provide adequate resolution in strategic areas, including near the wing leading and trailing edges. Based on the lessons learned, the following fixed-grid families have been selected for the HiFiCFD verification studies: mixed-element HM grid families designated at the HLPW-5 website as 1.R.03, 1.R.05, and 1.R.07 and a hex-dominated grid family 1.L.01 generated for hybrid RANS-LES by ANSA. Tables 5 and 6 show the corresponding grid statistics. In addition, solutions have been computed on families of adapted grids.

Table 5   Statistics of HM grid families

	1.R.03		1.R.05		1.R.07	
Grid	Grid points (millions)	Grid cells (millions)	Grid points (millions)	Grid cells (millions)	Grid points (millions)	Grid cells (millions)
Grid C	1.1	2.7	0.9	2.6	5.0	12.0
Grid M	7.6	18.4	5.8	17.8	13.4	31.2
Grid F	58.1	136.0	42.9	131.0	38.9	87.1
Grid R	N/A	N/A	331.2	1,010.0	105.6	232.4
Grid R+	N/A	N/A	N/A	N/A	191.0	415.1

Table 6   Statistics of ANSA grid family

	1.L.01	
Grid	Grid points (millions)	Grid cells (millions)
Grid A	5.8	7.0
Grid B	14.0	16.1
Grid C	37.5	42.0
Grid D	73.1	80.5
Grid E	187.5	202.4

B. Numerical Solutions

For the CRM-HL-WB configuration, six sets of solutions have been computed on fixed grid families and two sets of solutions have been computed on adapted grids. Grid convergence for the lift, drag, and pitching moment coefficients is shown in Fig. 30. In addition to solutions submitted to HiFiCFD, the figure shows two sets of solutions computed with the SA-neg-QCR2000-R model for HLPW-5. The additional sets include FUN3D solutions computed on the 1.R.05 grid family by Textron Aviation and a set of adaptive-grid solutions computed by a Boeing finite-element solver, GGNS-T1/EPIC. All solutions on all grids converged residuals to low levels and appear to be converging with grid refinement. There is a good agreement between aerodynamic forces approached in the limit of grid refinement. Considering solutions computed on the finest grids in each set, the lift, drag, and pitching-moment coefficients vary by less than 1%, 3% (18 drag counts), and 17%, respectively. If we exclude COFFE's solutions that trend in the right direction, but the grids appear to be too coarse, the variation becomes less than 0.5%, 0.8% (5 drag counts), and 8%, respectively. These levels of grid convergence are sufficient to clearly distinguish between aerodynamic coefficients computed from solutions with different variants of the SA turbulence model. Although not shown, solutions computed on preliminary HLPW-5 families of grids without sufficient residual reduction did not indicate grid convergence and did not agree to each other. A good agreement between solutions has been achieved only after the grid requirements to facilitate grid convergence have been understood and implemented, and the iterative convergence has been closely monitored. The main lessons learned from this verification exercise are the following:

- Grid convergence and deep iterative convergence are needed to establish agreement between solutions computed with the same RANS model by different solvers on different families of grids.
- Well designed families of grids that strategically place degrees of freedom in important areas are critical for achieving grid convergence with reasonably small degrees of freedom.
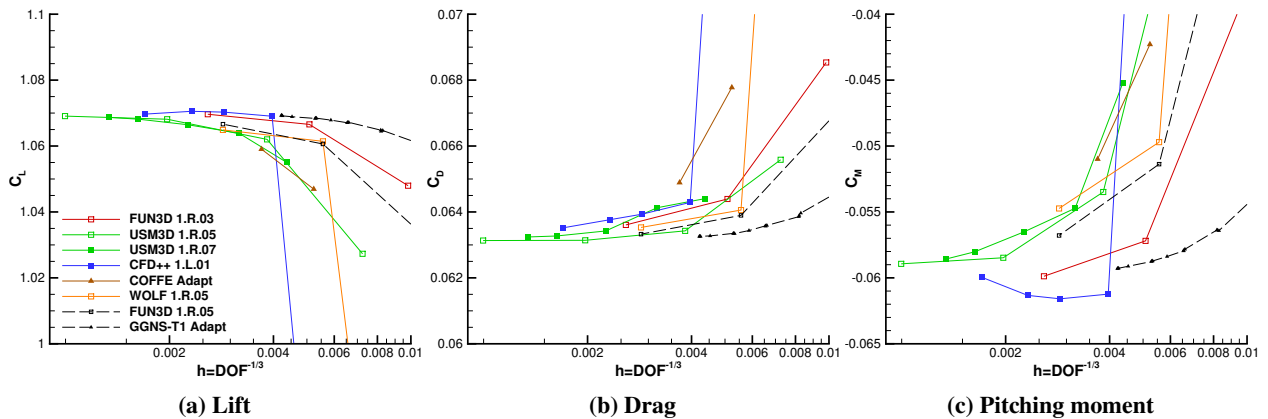

(a) Lift   (b) Drag   (c) Pitching moment

Fig. 30   CRM-HL-WB solutions

VII. Summary

The High-Fidelity Computational Fluid Dynamics (CFD) Verification Workshop (HiFiCFD) includes four test suites for verification of different models relevant for modern CFD solvers. This paper reports on international collaboration focusing on verification of Reynolds-averaged Navier-Stokes (RANS) solvers with a Spalart-Allmaras turbulence model enhanced with the ability to handle negative working variables, quadratic constitutive relation, and rotation correction. The model is designated as the SA-neg-QCR2000-R model at the NASA Turbulence Modeling Resource (TMR) website. The rotation correction (designated as –R) is used to mitigate the generation of spurious eddy viscosity within mature vortices.

For almost two years, researchers from major government laboratories, industry, academia, and software vendors conducted regular bi-weekly meetings and intensely collaborated using seven established CFD solvers to compute and compare solutions on multiple families of expert-generated and solution-adapted grids. The solvers used in the verification study are `FUN3D` and `USM3D-ME` (NASA Langley Research Center), `COFFE` from HPCMP CREATE™-AV Kestrel, `CFD++` (Metacomp Technologies, Inc.), `SANS` (MIT), `WOLF` (INRIA, France), and an open-source toolbox, `OpenFOAM`. These solvers use various discretization approaches including cell-centered and node-centered, finite-volume and finite-element, second- and high-order discretizations. The grid families were generated by `HeldenMesh`™ (HM) software developed at Helden Aerospace, Inc., Cadence® software `Pointwise`™ (PW), and MIT's Metric Optimization via Error Sampling and Synthesis (MOESS) grid adaptation framework. In addition, two series of adapted grids were generated using `WOLF`, but these grids were used only by `WOLF`. The main contributions of this paper are a detailed description of the SA-neg-QCR2000-R turbulence model and the three test cases of progressive complexity for its verification. For each test case, the grids, boundary and flow conditions, and reference solutions are described in detail.

The first test case is a two-dimensional (2D) flow around the Joukowski airfoil. This is a simple verification case designed to demonstrate the optimal grid-convergence rate. A family of uniformly-refined nested quadrilateral grids has been generated for the study. The finest grid in the family includes more than 3 million grid nodes. In addition, three families of adapted grids have been generated by MOESS. Thirteen sets of solutions have been computed. All solutions reduced residuals to machine-zero levels on all grids and converged toward each other with grid refinement. The variation of the total-drag coefficient on the finest grids in the families is less than 1%. The high-order solutions and solutions on adapted grids show better accuracy per degree of freedom than second-order solutions on fixed grids.

An internal flow around an extruded NACA 0012 wing mounted on a tunnel wall is the main verification case for the SA-neg-QCR2000-R turbulence model. This case features a simple wing in a tunnel that produces a tip vortex. A similar geometry was used in the original paper that introduced the rotation correction. For ease of verification, the geometry in this paper was slightly modified and a simplified set of boundary conditions was imposed in hope to observe grid-converged solutions on coarser grids. The geometry modifications include upstream and downstream extensions of the test section to minimize singularities and a converged tunnel downstream of the wing to avoid reverse flow at the outflow boundary. The simplified boundary conditions include the viscous-wall condition for the wing and the mounting wall within the test section and the tangency-wall conditions on all other surfaces. The HM, PW, and MOESS grid families were generated for this geometry. The degrees of freedom provided by the fixed grids range from just under one million to over 500 million. The MOESS adapted grids provide from 20 thousand to above 3 million degrees of freedom. `WOLF` adapted grids provide up to 2.5 million degrees of freedom. Fifteen solution sets were computed and reported the total-lift, total-drag, pressure-drag, and viscous-drag coefficients. The aerodynamic coefficients from almost all solutions appear converging to the same limit with grid refinement. Excluding one solver, the variation of the total-lift coefficients computed by different solvers on the finest grids in the families was less than 0.3%; the variation of the drag coefficient was less than 2 drag counts or less than 2%. The variation can be further reduced if grids with more degrees of freedom are provided.

The variations of the pressure and x-component of skin friction were observed at two wing cross-sections parallel to the xz-coordinate plane: one cross-section is close to the wing-wall juncture, another cross-section is close to the wing tip. In global views, the section pressure- and skin-friction coefficients appear converged on the HM and PW grids and on the `WOLF`'s adapted grids. On the MOESS grids, the section pressure coefficient appears converged but the skin-friction coefficient appears noisy. When section plots obtained on the finest grids in corresponding families were plotted together, significant differences were observed near the suction peak. Apparently, higher grid resolution is required to achieve better grid convergence.

The effect of the rotation correction on the vortex core has been observed in two cross-sections parallel to the yz coordinate plane; one is located in the immediate proximity to the trailing edge and the other is placed far downstream beyond the test section. As expected, significant reduction of the turbulent eddy viscosity within the vortex core has been observed, but even stronger reduction is needed to prevent spurious vortex dissipation. Grid convergence of

the turbulence working variable within the vortex core has not been established. Good agreement between different solutions has been established for the location near the wing, but poor agreement was observed for the downstream location. The vortex core representation at the downstream location has been found sensitive to grid resolution; the resolution provided by the available grids is not sufficient.

The third and most realistic test case is a flow around a simplified wing-body high-lift common research model (CRM-HL-WB). This case is a common verification case with the Fifth High-Lift Prediction Workshop (HLPW-5). For this case, four fixed-grid families generated for the HLPW-5 have been used. Six sets of solutions have been computed on theses grids. In addition, COFFE computed solutions on two adapted grids, and another set of solutions on adapted grids was contributed by Boeing's code GGNS-T1. All solutions converged residuals on all grids to machine-zero levels. The lift, drag, and pitching moment coefficients computed by different solvers have been monitored and agree in grid refinement. Considering the SA-neg-QCR2000-R solutions computed by different solvers on the fine grids in the families, the variation between the lift, drag, and pitching moment coefficients becomes less than 0.5%, 0.8% (5 drag counts), and 8%, respectively. Collaborative studies conducted together with the HLPW-5 participants concluded that CRM-HL-WB solutions computed by different solvers on different grid families (but corresponding to the same RANS model) can converge with grid refinement provided we have well designed grid families that place sufficient degrees of freedom in important areas and strong iterative solvers capable of deep iterative convergence on each grid in the family.

Appendices

A. Drag Trend in the Low-Mach Limit

In addition to the workshop's mandatory grid-convergence study, CFD++ used the Joukowski-airfoil geometry to examine the drag trend in the low-Mach limit. Figure 31 shows variation of the total-, viscous-, and pressure-drag coefficients versus Mach number squared from the incompressible limit ($M = 0$) to Mach $M = 0.5$. Figure 32 shows residual convergence for solutions corresponding to selected Mach number. The viscous drag coefficient increases (roughly linearly with M^2) with increasing Mach number, while the pressure drag decreases (again, roughly linearly with M^2) over the same interval. The total drag at these low Mach numbers is dominated by viscous drag, however, the pressure drag exhibits larger change with M^2, and thus the overall trend for the total drag is decreasing with M^2. Separate inviscid simulations showed extremely low pressure-drag coefficient, confirming that, for this symmetric airfoil flow, the pressure drag component exists only as a result of viscosity.
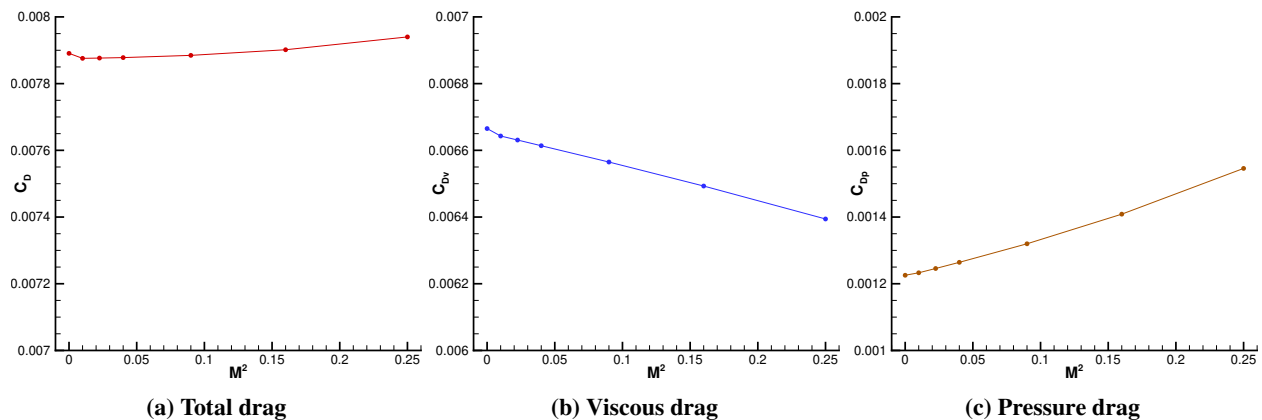

(a) Total drag   (b) Viscous drag   (c) Pressure drag

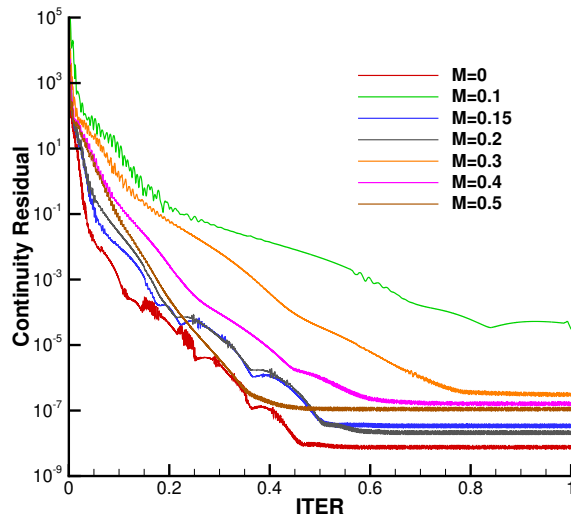Fig. 31   Low-Mach drag trend as a function of Mach squared

Fig. 32   Residual Convergence

B. Effect of Tunnel Slip-Wall Boundary Conditions

In addition to the mandatory grid-convergence study for the NACA 0012 wing in tunnel, an additional study was made using the CFD++ solver to assess the impact of the requested tangency (slip-wall) boundary condition on the three walls of the tunnel section (the no-slip viscous-wall boundary conditions are used for the wing and the mounting wall of the test section of the tunnel). These slip-wall boundary conditions can be considered as flow conditions in which the normal-to-boundary velocity components vanish at the boundary, but tangential velocities do not. This would correspond, for example, to the situation at a free-surface where only one of the three normal-stresses in the surface-coordinate-aligned frame would vanish. Clearly, this situation cannot be represented exactly in an isotropic eddy viscosity model, hence this slip approach is considered as an artificial approximation, whereby the meanflow near the wall is treated as inviscid (slip wall), but the eddy viscosity itself is set to zero on the slip wall. CFD++ actually does not currently have such a slip-wall boundary condition as an option, however, with sufficient mesh resolution this boundary condition is directly implied in the SA model at the slip surface via its decay term.

Two sets of computations were made using the NACA 0012 geometry and PW, NM, and MOESS grid families described in the main-body Section V. For each of these grid families, slip-wall conditions were imposed on the meanflow variables. A study was conducted, in which wall distances were once computed as requested to all walls (Slip), and, then, a standard wall-distance (SWD) boundary condition were imposed, in which wall distances were computed only to the no-slip walls, i.e., the wing surface itself and the vertical side wall to which the wing is mounted.
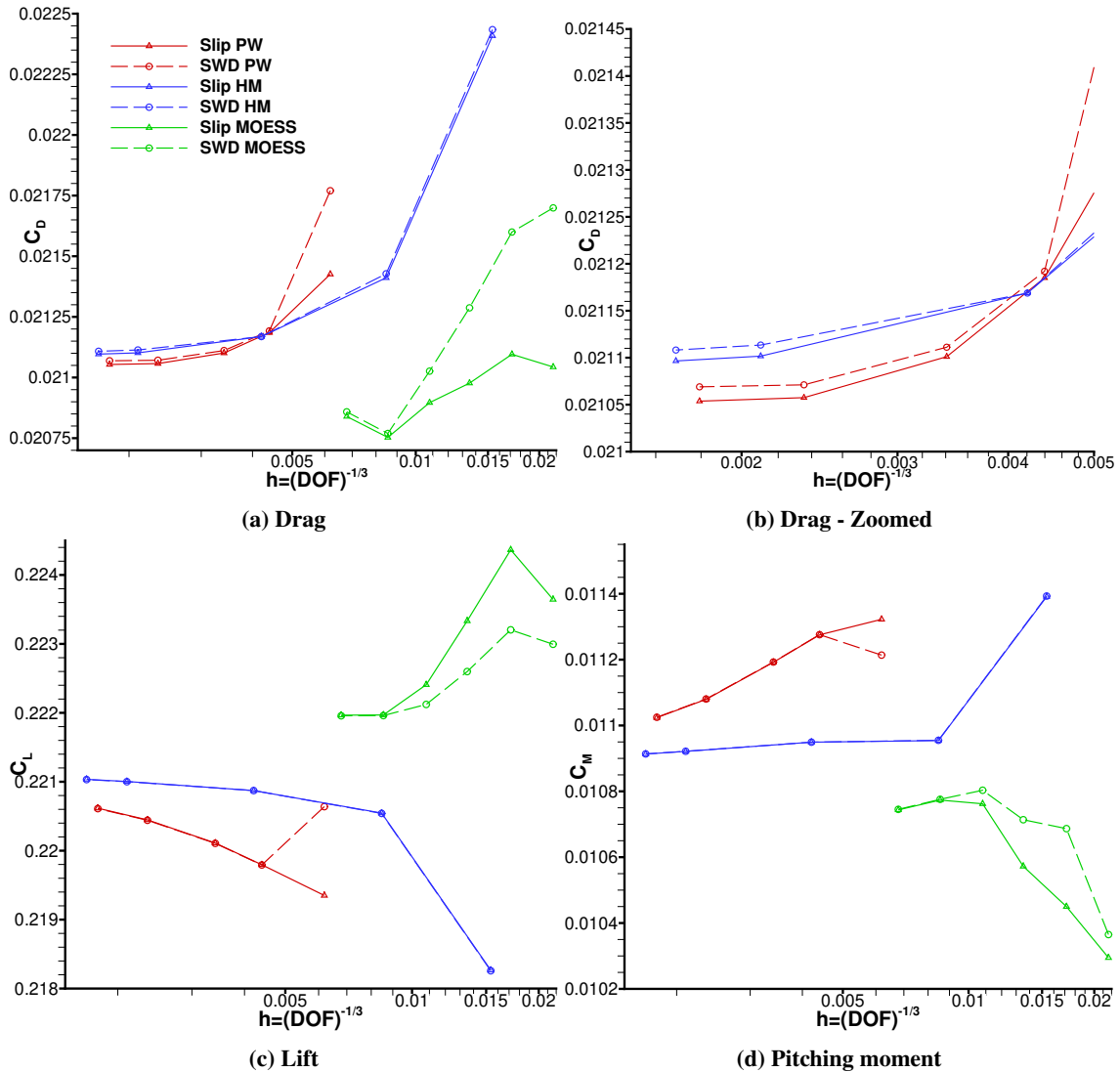
Fig. 33 Comparison of Slip vs Standard Inviscid/Symmetry (SWD) Boundary Conditions

Figure 33 shows the comparison of the force and moment coefficients computed using the "Slip" and "SWD" boundary approaches. The limit of grid refinement appears to show no differences between the SWD boundary condition and the requested Slip boundary conditions. However, at the level of detail being sought in this grid-convergence effort, the limits are not exactly the same, as seen in the zoomed-in plot for the drag coefficient in Figure 33b. Close reproduction of the results shown in this paper requires the use of the Slip boundary condition in the SA-neg-QCR2000-R model.

References

[1] "High Fidelity CFD Workshop 2022," `https://turbmodels.larc.nasa.gov/highfidelitycfd_workshop2022.html`, 2022. Accessed: 2024-05-17.

[2] "4th International Workshop on High-Order CFD Methods," `https://how4.cenaero.be`, 2016. Accessed: 2024-05-17.

[3] "5th International Workshop on High-Order CFD Methods," `https://how5.cenaero.be`, 2018. Accessed: 2024-05-17.

[4] Diskin, B., and Thomas, J. L., "Introduction: Evaluation of RANS Solvers on Benchmark Aerodynamic Flows," *AIAA Journal*, Vol. 54, No. 9, 2016, pp. 2561, 2562. https://doi.org/10.2514/1.J054642.

[5] Diskin, B., Anderson, W. K., Pandya, M. J., Rumsey, C. L., Thomas, J. L., Liu, Y., and Nishikawa, H., "Grid Convergence of Three-Dimensional Benchmark Turbulent Flows," *AIAA Paper 2018–1102*, January 2018. https://doi.org/10.2514/6.2018-1102.

[6] "Turbulence Modeling Resource," https://turbmodels.larc.nasa.gov, 2022. Accessed: 2024-05-17.

[7] Allmaras, S. R., Johnson, F. T., and Spalart, P. R., "Modifications and Clarifications for the Implementation of the Spalart-Allmaras Turbulence Model," *Seventh International Conference on Computational Fluid Dynamics (ICCFD7),* ICCFD7-1902, 2012. URL https://www.iccfd.org/iccfd7/assets/pdf/papers/ICCFD7-1902_paper.pdf.

[8] Spalart, P. R., and Allmaras, S. R., "A One-Equation Turbulence Model for Aerodynamic Flows," *Recherche Aerospatiale,* No. 1, 1994, pp. 5–21. URL https://turbmodels.larc.nasa.gov/Papers/RechAerosp_1994_SpalartAllmaras.pdf.

[9] Diskin, B., Thomas, J. L., Rumsey, C. L., and Schwöppe, A., "Grid-Convergence of Reynolds-Averaged Navier–Stokes Solutions for Benchmark Flows in Two Dimensions," *AIAA Journal*, Vol. 54, No. 9, 2016, pp. 2563–2588. https://doi.org/10.2514/1.J054555.

[10] Spalart, P. R., "Strategies for Turbulence Modelling and Simulation," *International Journal of Heat and Fluid Flow*, Vol. 21, No. 3, 2000, pp. 255–263. https://doi.org/10.1016/S0142-727X(00)00007-2.

[11] Diskin, B., Ahmad, N., Anderson, W. K., Derlaga, J. M., Pandya, M. J., Rumsey, C. L., Wang, L., Wood, S. L., Liu, Y., Nishikawa, H., and Galbraith, M. C., "Verification Test Suite for Spalart-Allmaras QCR2000 Turbulence Model," *AIAA Paper 2021–1552*, January 2021. https://doi.org/10.2514/6.2021-1552.

[12] Rumsey, C. L., "The NASA Juncture Flow Test as a Model for Effective CFD/Experimental Collaboration," *AIAA Paper 2018–3319*, June 2018. https://doi.org/10.2514/6.2018-3319.

[13] Dacles-Mariani, J., Zilliac, G. G., Chow, J. S., and Bradshaw, P., "Numerical/Experimental Study of a Wingtip Vortex in the Near Field," *AIAA Journal*, Vol. 33, No. 9, 1995, pp. 1561–1568. https://doi.org/10.2514/3.12826.

[14] Dacles-Mariani, J., Kwak, D., and Zilliac, G. G., "On Numerical Errors and Turbulence Modeling in Tip Vortex Flow Prediction," *International Journal for Numerical Methods in Fluids*, Vol. 30, No. 1, 1999, pp. 65–82. https://doi.org/10.1002/(SICI)1097-0363(19990515)30:1<65::AID-FLD839>3.0.CO;2-Y.

[15] Alauzet, F., and Spalart, P. R., "A New Rotation Correction for the Spalart-Allmaras Model to Improve Off-Body Vortex Prediction and Vortex-Vortex Interaction Effects," *AIAA Paper 2024–1335*, January 2024. https://doi.org/10.2514/6.2024-1335.

[16] "Fifth AIAA CFD High-Lift Prediction Workshop (HLPW-5)," https://hiliftpw.larc.nasa.gov/, 2024. Accessed: 2024-05-17.

[17] "High-Fidelity CFD Verification Workshop," https://highfidelitycfdverificationworkshop.github.io/, 2024. Accessed: 2024-05-17.

[18] Diskin, B., Liu, Y., and Galbraith, M. C., "High-Fidelity CFD Verification Workshop 2024: Spalart-Allmaras QCR2000-R Turbulence Model," *AIAA Paper 2023–1244*, 2023. https://doi.org/10.2514/6.2023-1244.

[19] Diskin, B., Pandya, M. J., Pomeroy, B. W., and Boyett, T. K., "Toward Verification of USM3D Extensions for Mixed Element Grids," *AIAA Paper 2023–3252*, 2023. https://doi.org/10.2514/6.2023-3252.

[20] Murayama, M., Ito, Y., Furuya, R., and Tanaka, K., "High-Fidelity CFD Verification Workshop 2024: Spalart-Allmaras QCR2000-R Turbulence Model," *AIAA Paper 2022–3743*, 2022. https://doi.org/10.2514/6.2022-3743.

[21] Peroomian, O., and Chakravarthy, S., "A Grid-Transparent Methodology for CFD," *AIAA Paper 97-00724*, 1997.

[22] Glasby, R. S., Erwin, J. T., Stefanski, D. L., Allmaras, S. R., Galbraith, M. C., Anderson, W. K., and Nichols, R. H., "Introduction to COFFE: The Next-Generation HPCMP CREATE(TM)-AV CFD Solver," *AIAA Paper 2016–0567*, January 2016. https://doi.org/10.2514/6.2016-0567.

[23] Hughes, T. J. R., "A Simple Scheme for Developing 'Upwind' Finite Elements," *International Journal for Numerical Methods in Engineering*, Vol. 12, No. 9, 1978, pp. 1359–1365. https://doi.org/10.1002/nme.1620120904.

[24] Brooks, A. N., and Hughes, T. J., "Streamline Upwind/Petrov-Galerkin Formulations for Convection Dominated Flows with Particular Emphasis on the Incompressible Navier-Stokes Equations," *Computer Methods in Applied Mechanics and Engineering*, Vol. 32, No. 1-3, 1982, pp. 199–259. https://doi.org/10.1016/0045-7825(82)90071-8.

[25] Bonhaus, D. L., "A Higher Order Accurate Finite Element Method for Viscous Compressible Flows," Ph.D. thesis, Virginia Polytechnic Institute and State University, 1998.

[26] Venkatakrishnan, V., Allmaras, S. R., Kamenetskii, D., and Johnson, F., "Higher Order Schemes for the Compressible Navier-Stokes Equations," *AIAA Paper 2003–3987*, June 2003. https://doi.org/10.2514/6.2003-3987.

[27] Erwin, J. T., Wang, L., Anderson, W. K., and Kapadia, S., "High-Order Finite-Element Method for Three-Dimensional Turbulent Navier-Stokes," *AIAA Paper 2013–2571*, June 2013. https://doi.org/10.2514/6.2013-2571.

[28] Anderson, W. K., Newman, J. C., and Karman, S. L., "Stabilized Finite Elements in FUN3D," *Journal of Aircraft*, Vol. 55, No. 2, 2018, pp. 696–714. https://doi.org/10.1016/0045-7930(94)90023-X.

[29] Holst, K. R., Glasby, R. S., Erwin, J. T., Stefanski, D. L., and Bond, R. B., "High-Order Time-Accurate Simulations using HPCMP CREATE(TM)-AV Kestrel Component COFFE," *AIAA Paper 2018–0027*, January 2018. https://doi.org/10.2514/6.2018-0027.

[30] Holst, K. R., Glasby, R. S., and Bond, R. B., "On the Effect of Temporal Error in High-Order Simulations of Unsteady Flows," *Journal of Computational Physics*, Vol. 402, 2020, p. 108989. https://doi.org/10.1016/j.jcp.2019.108989.

[31] Saad, Y., and Schultz, M. H., "GMRES: A Generalized Minimal Residual Algorithm for Solving Nonsymmetric Linear Systems," *SIAM Journal on Scientific and Statistical Computing*, Vol. 7, No. 3, 1986, pp. 856–869. https://doi.org/10.1137/0907058.

[32] Anderson, W. K., Biedron, R. T., Carlson, J.-R., Derlaga, J. M., Diskin, B., Jr., C. T. D., Gnoffo, P. A., Hammond, D. P., Jacobson, K. E., Jones, W. T., Kleb, B., Lee-Rausch, E. M., Liu, Y., Nastac, G. C., Nielsen, E. J., Padway, E. M., Park, M. A., Rumsey, C. L., Thomas, J. L., Thompson, K. B., Walden, A. C., Wang, L., Wood, S. L., Wood, W. A., and Zhang, X., "FUN3D Manual: 14.0.2," Tech. rep., NASA TM 20230004211, 2023.

[33] Nielsen, E. J., and Diskin, B., "High-Performance Aerodynamic Computations for Aerospace Applications," *Parallel Computing*, Vol. 64, 2017, pp. 20–32. https://doi.org/10.1016/j.parco.2017.02.004.

[34] Wang, L., Diskin, B., Lopes, L. V., Nielsen, E. J., Lee-Rausch, E., and Biedron, R. T., "High-Fidelity Aero-Acoustic Optimization Tool for Flexible Rotors," *Journal of the American Helicopter Society*, Vol. 66, No. 2, 2021, pp. 1–16. https://doi.org/10.4050/JAHS.66.022004.

[35] Ordaz, I., Nielsen, E. J., Rallabhandi, S. K., and Diskin, B., "Adjoint-Based Design of a Distributed Propulsion Concept with a Power Objective," *AIAA Paper 2019–3861*, June 2019. https://doi.org/10.2514/6.2019-3861.

[36] Nastac, G. C., Walden, A. C., and Nielsen, E. J., "Implicit Thermochemical Nonequilibrium Flow Simulations on Unstructured Grids Using GPUs," *AIAA Paper 2021–0159*, January 2021. https://doi.org/10.2514/6.2021-0159.

[37] Nastac, G. C., Walden, A. C., Wang, L., Nielsen, E. J., Liu, Y., Opgenorth, M., Orender, J., and Zubair, M., "A Multi-Architecture Approach for Implicit Computational Fluid Dynamics on Unstructured Grids," *AIAA Paper 2023–1226*, January 2023. https://doi.org/10.2514/6.2023-1226.

[38] Nastac, G. C., Ernst, Z., Hickey, A. M., Walden, A. C., Jacobson, K. E., Jones, W. T., Nielsen, E. J., Diskin, B., Wang, L., Korzun, A. M., Moran, P. J., Dean, H. V., Robertson, B. E., and Mavris, D., "Closed-Loop Simulations of Human-Scale Mars Lander Descent Trajectories on Frontier," *AIAA Paper 2024–*****, July 2024. https://doi.org/10.2514/6.2024-****.

[39] Anderson, W. K., and Bonhaus, D. L., "An Implicit Upwind Algorithm for Computing Turbulent Flows on Unstructured Grids," *Computers and Fluids*, Vol. 23, No. 1, 1994, pp. 1–21. https://doi.org/10.1016/0045-7930(94)90023-X.

[40] Roe, P. L., "Approximate Riemann Solvers, Parameter Vectors, and Difference Schemes," *Journal of Computational Physics*, Vol. 43, No. 2, 1981, pp. 357–372. https://doi.org/10.1016/0021-9991(81)90128-5.

[41] van Leer, B., "Towards the Ultimate Conservative Difference Scheme, V:A Second Order Sequel to Godunov's Method," *Journal of Computational Physics*, Vol. 32, No. 1, 1979, pp. 101–136. https://doi.org/10.1016/0021-9991(79)90145-1.

[42] Burg, C. O. E., "Higher Order Variable Extrapolation for Unstructured Finite Volume RANS Flow Solvers," *AIAA Paper 2005–4999*, 2005. https://doi.org/10.1016/0021-9991(81)90128-5.

[43] Barth, T. J., "Numerical Aspects of Computing Viscous High Reynolds Number Flows on Unstructured Meshes," *AIAA Paper 1991–721*, 1991. https://doi.org/10.2514/6.1991-721.

[44] Haselbacher, A. C., "A Grid-Transparent Numerical Method for Compressible Viscous Flow on Mixed Unstructured Meshes," Phd thesis, Loughborough University, Loughborough, England, U.K., December 1998. Available at https://hdl.handle.net/2134/7257.

[45] Nishikawa, H., "Beyond Interface Gradient: A General Principle for Constructing Diffusion Schemes," *AIAA Paper 2010–5093*, 1991. https://doi.org/10.2514/6.2010-5093.

[46] Thomas, J. L., Diskin, B., and Nishikawa, H., "A Critical Study of Agglomerated Multigrid Methods for Diffusion on Highly Stretched Grids," *Computers and Fluids*, Vol. 41, No. 1, 2001, pp. 82–93. https://doi.org/10.1016/j.compfluid.2010.09.023.

[47] Knoll, D. A., and Keyes, D. E., "Jacobian-Free Newton–Krylov Methods: A Survey of Approaches and Applications," *Journal of Computational Physics*, Vol. 193, No. 2, 2004, pp. 357–397. https://doi.org/10.1016/j.jcp.2003.08.010.

[48] Van der Vorst, H. A., and Vuik, C., "Jacobian-Free GMRESR: A Family of Nested GMRES Methods," *Numerical Linear Algebra with Applications*, Vol. 1, No. 4, 1994, pp. 369–386. https://doi.org/10.1002/nla.1680010404.

[49] Lucas, P., van Zuijlen, A. H., and Bijl, H., "Fast Unsteady Flow Computations with a Jacobian-Free Newton-Krylov Algorithm," *Journal of Computational Physics*, Vol. 229, No. 24, 2010, pp. 9201–9215. https://doi.org/10.1016/j.jcp.2010.08.033.

[50] Huang, A. C., Carson, H. A., Allmaras, S. R., Galbraith, M. C., Darmofal, D. L., and Kamenetskiy, D. S., "A Variational Multiscale Method with Discontinuous Subscales for Output-Based Adaptation of Aerodynamic Flows," *AIAA Paper 2020–1563*, January 2020. https://doi.org/10.2514/6.2020-1563.

[51] Huang, A. C., "An Adaptive Variational Multiscale Method with Discontinuous Subscales for Aerodynamic Flows," PhD thesis, Massachusetts Institute of Technology, Department of Aeronautics and Astronautics, Feb. 2020.

[52] Allmaras, S. R., Galbraith, M. C., and Wyman, N. J., "Output-based Mesh Adaptation Using Commercial Mesh Generation Software," *AIAA Paper 2022–4084*, 2022. https://doi.org/10.2514/6.2022-4084.

[53] Yano, M., and Darmofal, D. L., "An Optimization-Based Framework for Anisotropic Simplex Mesh Adaptation," *Journal of Computational Physics*, Vol. 231, No. 22, 2012, pp. 7626–7649. https://doi.org/10.1016/j.jcp.2012.06.040.

[54] Carson, H. A., Huang, A. C., Galbraith, M. C., Allmaras, S. R., and Darmofal, D. L., "Anisotropic mesh adaptation for continuous finite element discretization through mesh optimization via error sampling and synthesis," *Journal of Computational Physics*, Vol. 420, 2020, p. 109620. https://doi.org/10.1016/j.jcp.2020.109620.

[55] Carson, H. A., Huang, A. C., Galbraith, M. C., Allmaras, S. R., and Darmofal, D. L., "Mesh optimization via error sampling and synthesis: An update," *AIAA Paper 2020–0087*, January 2020. https://doi.org/10.2514/6.2020-0087.

[56] Carson, H. A., "Provably Convergent Anisotropic Output-Based Adaptation for Continuous Finite Element Discretizations," PhD thesis, Massachusetts Institute of Technology, Department of Aeronautics and Astronautics, Nov. 2019. URL https://dspace.mit.edu/handle/1721.1/129891.

[57] Becker, R., and Rannacher, R., "An Optimal Control Approach to A Posteriori Error Estimation in Finite Element Methods," *Acta Numerica*, Vol. 10, edited by A. Iserles, Cambridge University Press, 2001, pp. 1–102. https://doi.org/10.1017/S0962492901000010.

[58] Ursachi, C.-I., Galbraith, M. C., Allmaras, S. R., and Darmofal, D. L., "Output-Based Adaptive Reynolds-Averaged Navier–Stokes Higher-Order Finite Element Solutions on a Multielement Airfoil," *AIAA Journal*, Vol. 59, No. 7, 2021, pp. 2532–2545. https://doi.org/10.2514/1.J059968.

[59] Michal, T., and Krakos, J., "Anisotropic Mesh Adaptation through Edge Primitive Operations," *AIAA Paper 2012–159*, January 2012. https://doi.org/10.2514/6.2012-159.

[60] Alauzet, F., Li, X., Seol, E. S., and Shephard, M. S., "Parallel Anisotropic 3D Mesh Adaptation by Mesh Modification," *Engineering with Computers*, Vol. 21, No. 3, 2006, pp. 247–258. https://doi.org/10.1007/s00366-005-0009-3, URL https://doi.org/10.1007/s00366-005-0009-3.

[61] Park, M. A., "Adjoint-Based, Three-Dimensional Error Prediction and Grid Adaptation," *AIAA Journal*, Vol. 42, No. 9, 2004, pp. 1854–1862. https://doi.org/10.2514/1.10051.

[62] Caplan, P. C., "Four-Dimensional Anisotropic Mesh Adaptation for Spacetime Numerical Simulations," PhD thesis, Massachusetts Institute of Technology, Department of Aeronautics and Astronautics, Jun. 2019. URL https://hdl.handle.net/1721.1/122367.

[63] Pandya, M. J., Frink, N. T., Ding, E., and Parlette, E. B., "Toward Verification of USM3D Extensions for Mixed Element Grids," *AIAA Paper 2013–2541*, 2013. https://doi.org/10.2514/6.2013-2541.

[64] Pandya, M. J., Diskin, B., Thomas, J. L., and Frink, N. T., "Improved Convergence and Robustness of USM3D Solutions on Mixed Element Grids," *AIAA Journal*, Vol. 54, No. 9, 2016, pp. 2589–2610. https://doi.org/10.2514/1.J054545.

[65] Pandya, M. J., Diskin, B., Thomas, J. L., and Frink, N. T., "Assessment of USM3D Hierarchical Adaptive Nonlinear Iteration Method Preconditioners for Three-Dimensional Cases," *AIAA Journal*, Vol. 55, No. 10, 2017, pp. 3409–3424. https://doi.org/10.2514/1.J055823.

[66] Pandya, M. J., Jespersen, D. C., Diskin, B., Thomas, J. L., and Frink, N. T., "Efficiency of Mixed-Element USM3D for Benchmark Three-Dimensional Flows," *AIAA Journal*, Vol. 59, No. 8, 2021, pp. 2997–3011. https://doi.org/10.2514/1.J059720.

[67] Pandya, M. J., Jespersen, D. C., Diskin, B., Thomas, J. L., and Frink, N. T., "Verification and Scalability of Mixed-Element USM3D for Benchmark Three-Dimensional Flows," *AIAA Journal*, Vol. 59, No. 11, 2021, pp. 4719–4738. https://doi.org/10.2514/1.J060064.

[68] Pandya, M. J., Frink, N. T., Abdol-Hamid, K. S., Samareh, J. A., Parlette, E. B., and Taft, J. R., "Enhancements to TetrUSS for NASA Constellation Program," *Journal of Spacecraft and Rockets*, Vol. 49, No. 4, 2012, pp. 617–631. https://doi.org/10.2514/1.A32089.

[69] Bauer, S. X., Krist, S. E., and Compton, W. B., "Generation of the Ares I-X Flight Test Vehicle Aerodynamic Data Book and Comparison to Flight," *AIAA Paper 2011–0011*, 2011. https://doi.org/10.2514/6.2011-11.

[70] Abdol-Hamid, K. S., Ghaffari, F., and Parlette, E. B., "Ares I Vehicle Computed Turbulent Ascent Aerodynamic Data Development and Analysis," *Journal of Spacecraft and Rockets*, Vol. 49, No. 4, 2012, pp. 596–608. https://doi.org/10.2514/1.A32112.

[71] Warwick, G., "Lockheed Martin Refines Hybrid Wing-Body Airlifter Concept," *Aviation Week*, February 17, 2014.

[72] Wick, A. T., Hooker, J. R., and Zeune, C. H., "Integrated Aerodynamic Benefits of Distributed Propulsion," *AIAA Paper 2015–1500*, 2015. https://doi.org/10.2514/6.2015-1500.

[73] Hooker, J. R., Wick, A. T., Zeune, C. H., and Agelastos, A., "Over Wing Nacelle Installations for Improved Energy Efficiency," *AIAA Paper 2013–2920*, 2013. https://doi.org/10.2514/6.2013-2920.

[74] Pomeroy, B. W., and Selig, M. S., "Design of Airfoils to Mitigate Wake Bursting," *AIAA Paper 2017–1210*, 2017. https://doi.org/10.2514/6.2017-1210.

[75] Viken, S. A., Hunter, C. A., McMillin, S. N., Gatlin, G. M., Maldonado, D., Housman, J. A., Duensing, J. C., Jensen, J. C., and Kiris, C. C., "Comparison of Computational Predictions of the Mach 0.80 Transonic Truss-Braced Wing Configuration with Experimental Data," *NASA Technical Memorandum-20205007879*, 2022. https://doi.org/10.2514/6.2017-1210.

[76] Mitchell, C. R., "Improved Reconstruction Schemes for the Navier-Stokes Equations on Unstructured Meshes," *AIAA Paper 1994–0642*, 2017. https://doi.org/10.2514/6.1994-642.

[77] Frink, N. T., "Tetrahedral Unstructured Navier-Stokes Method for Turbulent Flows," *AIAA Journal*, Vol. 36, No. 11, 1998, pp. 1975–1982. https://doi.org/10.2514/2.324.

[78] Alauzet, F., and Loseille, A., "High-order Sonic Boom Modeling Based on Adaptive Methods," *Journal of Computational Physics*, Vol. 229, No. 3, 2010, pp. 561–593. https://doi.org/10.1016/j.jcp.2009.09.020.

[79] Menier, V., Loseille, A., and Alauzet, F., "CFD Validation and Adaptivity for Viscous Flow Simulations," *7th AIAA Theoretical Fluid Mechanics Conference*, AIAA, Atlanta, 2014, pp. 1–22. https://doi.org/10.2514/6.2014-2925, URL https://inria.hal.science/hal-01113355.

[80] Alauzet, F., and Frazza, L., "Feature-Based and Goal-Oriented Anisotropic Mesh Adaptation for RANS Applications in Aeronautics and Aerospace," *Journal of Computational Physics*, Vol. 439, 2021, p. 110340. https://doi.org/10.1016/j.jcp.2021.110340.

[81] Alauzet, F., Frazza, L., and Papadogiannis, D., "Periodic Adjoints and Anisotropic Mesh Adaptation in Rotating Frame for High-Fidelity RANS Turbomachinery Applications," *Journal of Computational Physics*, Vol. 450, 2022, p. 110814. https://doi.org/10.1016/j.jcp.2021.110814.

[82] Batten, P., Clarke, N., Lambert, C., and Causon, D. M., "On the Choice of Wavespeeds for the HLLC Riemann Solver," *SIAM Journal on Scientific Computing*, Vol. 18, No. 6, 1997, pp. 1553–1570. https://doi.org/10.1137/S1064827593260140.

[83] Stoufflet, B., Periaux, J., Fezoui, F., and Dervieux, A., "Numerical Simulation of 3-D Hypersonic Euler Flows around Space Vehicles using Adapted Finite Elements," *25th AIAA Aerospace Sciences Meeting*, AIAA, Reno,NV, 1987, p. 560. https://doi.org/10.2514/6.1987-560.

[84] Debiez, C., and Dervieux, A., "Mixed-Element-Volume MUSCL Methods with Weak Viscosity for Steady and Unsteady Flow Calculations," *Computers and Fluids*, Vol. 29, No. 1, 2000, pp. 89–118. https://doi.org/10.1016/S0045-7930(98)00059-0.

[85] Tarsia Morisco, C., Tenkès, L.-M., and Alauzet, F., "Vertex-Centered Mixed Finite Element–Finite Volume scheme for 2D anisotropic hybrid mesh adaptation," *Computer Methods in Applied Mechanics and Engineering*, Vol. 419, 2024, p. 116638. https://doi.org/10.1016/j.cma.2023.116638.

[86] Puigt, G., Auffray, V., and Müller, J.-D., "Discretisation of Diffusive Fluxes on Hybrid Grids," *Journal of Computational Physics*, Vol. 229, No. 5, 2010, pp. 1425–1447. https://doi.org/10.1016/j.jcp.2009.10.037.

[87] Tarsia Morisco, C., Tenkes, L.-M., and Alauzet, F., "Extension of the Vertex-Centered Mixed-Element-Volume MUSCL scheme to mixed-element meshes," *AIAA Paper 2023–0832*, January 2023. https://doi.org/10.2514/6.2023-0832.

[88] Tarsia Morisco, C., and Alauzet, F., "Validation of the Spalart-Allmaras QCR2000-R Turbulence Model using Anisotropic Mesh Adaptation on HFCFDV Workshop Test Cases," *AIAA Paper 2024–2741*, January 2024. https://doi.org/10.2514/6.2024-2741.

[89] Alauzet, F., and Loseille, A., "A Decade of Progress on Anisotropic Mesh Adaptation for Computational Fluid Dynamics," *Computer-Aided Design*, Vol. 72, 2016, pp. 13–39. https://doi.org/10.1016/j.cad.2015.09.005.

[90] Loseille, A., and Alauzet, F., "Continuous Mesh Framework Part I: Well-Posed Continuous Interpolation Error," *SIAM Journal on Numerical Analysis*, Vol. 49, No. 1, 2011, pp. 38–60. https://doi.org/10.1137/090754078.

[91] Loseille, A., and Alauzet, F., "Continuous Mesh Framework Part II: Validations and Applications," *SIAM Journal on Numerical Analysis*, Vol. 49, No. 1, 2011, pp. 61–86. https://doi.org/10.1137/10078654X.

[92] Borouchaki, H., Hecht, F., and Frey, P. J., "Mesh Gradation Control," *International Journal for Numerical Methods in Engineering*, Vol. 43, 1999, p. 1143–1165. https://doi.org/10.1002/(SICI)1097-0207(19981130)43:6<1143::AID-NME470>3.0.CO;2-I.

[93] Alauzet, F., "Size Gradation Control of Anisotropic Meshes," *Finite Elements in Analysis and Design*, Vol. 46, 2010, pp. 1–2. https://doi.org/10.1016/j.finel.2009.06.028.

[94] Loseille, A., and Löhner, R., "On 3D Anisotropic Local Remeshing for Surface, Volume and Boundary Layers," *Proceedings of the 18th international meshing roundtable*, Springer, Salt Lake City, UT, 2009, pp. 611–630.

[95] Loseille, A., and Lohner, R., "Anisotropic Adaptive Simulations in Aerodynamics," *48th AIAA Aerospace Sciences Meeting Including the New Horizons Forum and Aerospace Exposition*, AIAA, Orlando, FL, January 2010, p. 169. https://doi.org/10.2514/6.2010-169.

[96] Loseille, A., and Lohner, R., "Boundary Layer Mesh Generation and Adaptivity," *49th AIAA Aerospace Sciences Meeting Including the New Horizons Forum and Aerospace Exposition*, AIAA, Orlando, FL, January 2011, p. 894. https://doi.org/10.2514/6.2011-894.

[97] Alauzet, F., and Mehrenberger, M., "P1-Conservative Solution Interpolation on Unstructured Triangular Meshes," *International Journal for Numerical Methods in Engineering*, Vol. 84, 2010, p. 1552–1588. https://doi.org/10.1002/nme.2951.

[98] Alauzet, F., "A Parallel Matrix-Free Conservative Solution Interpolation on Unstructured Tetrahedral Meshes," *Computer Methods in Applied Mechanics and Engineering*, Vol. 299, 2016, pp. 116–142. https://doi.org/10.1016/j.cma.2015.10.012.

[99] Alauzet, F., Clerici, F., Loseille, A., Tarsia Morisco, C., and Vanharen, J., "Some Progress on CFD High Lift Prediction Using Metric-Based Anisotropic Mesh Adaptation," *AIAA Paper 2022–0388*, January 2022. https://doi.org/10.2514/6.2022-0388.

[100] Jasak, H., "OpenFOAM: Open Source CFD in Research and Industry," *International Journal of Naval Architecture and Ocean Engineering*, Vol. 1, No. 2, 2009, pp. 89–94. https://doi.org/10.2478/IJNAOE-2013-0011.

[101] Caretto, L., Gosman, A., Patankar, S., and Spalding, D., "Two Calculation Procedures for Steady, Three-Dimensional Flows With Recirculation," *Proceedings of the Third International Conference on Numerical Methods in Fluid Mechanics*, Lecture Notes in Physics, Vol. 19, 1972, pp. 60–68. https://doi.org/10.1007/BFb0112677.

[102] Issa, R. I., "Solution of the Implicitly Discretized Fluid Flow Equations by Operator-Splitting," *Journal of Computational Physics*, Vol. 62, No. 1, 1986, pp. 40–65. https://doi.org/10.1016/0021-9991(86)90099-9.

[103] Heyns, J. A., Oxtoby, O. F., and Steenkamp, A., "Modelling High-Speed Flow Using a Matrix-Free Coupled Solver," *Proceedings of the 9th OpenFOAM Workshop, Zagreb, Croatia*, 2014, pp. 23–26.

[104] Liou, M.-S., "A Sequel to AUSM, Part II: AUSM+-up for All Speeds," *Journal of Computational Physics*, Vol. 214, No. 1, 2006, pp. 137–170. https://doi.org/10.1016/j.jcp.2005.09.020.

[105] Toro, E. F., "The HLLC Riemann Solver," *Shock waves*, Vol. 29, No. 8, 2019, pp. 1065–1082. https://doi.org/10.1007/s00193-019-00912-4.

[106] Warming, R. F., and Beam, R. M., "Upwind Second-Order Difference Schemes and Applications in Aerodynamic Flows," *AIAA Journal*, Vol. 14, No. 9, 1976, pp. 1241–1249. https://doi.org/10.2514/3.61457.

[107] "HeldenMesh Website," https://heldenaero.com/heldenmesh/, 2024. Accessed: 2024-05-17.

[108] Karman, S. L., and Wyman, N. J., "Automatic Unstructured Mesh Generation with Geometry Attribution," *AIAA Paper 2019–1721*, 2019. https://doi.org/10.2514/6.2019-1721.

[109] Lacy, D. S., and Clark, A. M., "Definition of Initial Landing and Takeoff Reference Configurations for the High Lift Common Research Model (CRM-HL)," *AIAA Paper 2020–2771*, 2020. https://doi.org/10.2514/6.2020-2771.